© 2020. Published by The Company of Biologists Ltd | Development (2020) 147, dev185231. doi:10.1242/dev.185231

RESEARCH ARTICLE

Neural crest cells bulldoze through the microenvironment using Aquaporin 1 to stabilize filopodia

Rebecca McLennan[1], Mary C. McKinney[1], Jessica M. Teddy[1], Jason A. Morrison[1], Jennifer C. Kasemeier-Kulesa[1], Dennis A. Ridenour[1], Craig A. Manthe[1], Rasa Giniunaite[2], Martin Robinson[2,3], Ruth E. Baker[2], Philip K. Maini[2] and Paul M. Kulesa[1,4,*]

ABSTRACT

Neural crest migration requires cells to move through an environment filled with dense extracellular matrix and mesoderm to reach targets throughout the vertebrate embryo. Here, we use high-resolution microscopy, computational modeling, and *in vitro* and *in vivo* cell invasion assays to investigate the function of Aquaporin 1 (AQP-1) signaling. We find that migrating lead cranial neural crest cells express AQP-1 mRNA and protein, implicating a biological role for water channel protein function during invasion. Differential AQP-1 levels affect neural crest cell speed and direction, as well as the length and stability of cell filopodia. Furthermore, AQP-1 enhances matrix metalloprotease activity and colocalizes with phosphorylated focal adhesion kinases. Colocalization of AQP-1 with EphB guidance receptors in the same migrating neural crest cells has novel implications for the concept of guided bulldozing by lead cells during migration.

KEY WORDS: Cell invasion, Filopodia, Neural crest, Water channel

INTRODUCTION

Cell migration is essential during embryogenesis in order to gastrulate, elongate the vertebrate axis and distribute cells into the periphery to contribute to organ development. Despite the importance of cell migration to human development and disease, it is still unclear what mechanisms enable cells to invade the dense extracellular matrix (ECM), mesoderm and other cell types characteristic of the embryonic microenvironment. The complexity of the embryonic microenvironment means that invading cells must rapidly change cell shape, form and sustain protrusions that penetrate different sized gaps, and attach to and remodel the ECM. Thus, there is a tremendous need to identify and test the function of molecules that are crucial to embryonic cell migration, and to better understand their mechanistic basis.

Neural crest cell migration is one of the most prevalent examples of how cells efficiently distribute throughout the growing vertebrate embryo to precise targets. In the head, cranial neural crest cells must invade through dense ECM, loosely connected mesoderm and migrating endothelial cells. Yet it has remained unclear how the migrating neural crest cells that first encounter the embryonic microenvironment penetrate small gaps between mesodermal cells and degrade the ECM to move in a directed manner to peripheral targets. By combining dynamic *in vivo* imaging and super resolution microscopy with gain- and loss-of-function experiments, we are poised to examine the function of genes presumed to be crucial to neural crest cell migration. Thus, the embryonic neural crest is an attractive *in vivo* model for studying the function of cell invasion genes in mechanistic detail.

Using single cell RT-qPCR and transcriptome profiling, we discovered the enhanced expression of several genes in the most invasive chick cranial neural crest cells, including Aquaporin 1 (*AQP-1*) (McLennan et al., 2015a; Morrison et al., 2017a). AQP-1 is a transmembrane channel protein that facilitates the flux of water across the plasma membrane (Agre et al., 1993) and is one member of a family of at least 13 aquaporins (Ishibashi et al., 2011). AQP-1 has been detected in several aggressive human cancers and its expression correlates with poor disease prognosis (Tomita et al., 2017; De leso and Yool, 2018). However, the mechanistic basis of AQP-1 function is still unclear because studies have been limited to analyzing cell behaviors using *in vitro* assays. This has led to the generation of several distinct hypothetical mechanisms for AQP-1 function. For example, AQP-1 is thought to allow cells to rapidly change cell volume to form thin filopodial protrusions that squeeze in between neighboring cells (Papadopoulos et al., 2008; Verkman, 2009; Karlsson et al., 2013) or to collapse a cell protrusion and cause it to retreat from a repulsive signal (Cowan et al., 2000). Alternatively, AQP-1 may function to stabilize a filopodia as aquaporins have been shown *in vitro* to localize to the front end of migrating cells (Saadoun et al., 2005) and are speculated to function as a cell motility engine (Condeelis, 1993; Stroka et al., 2014). Thus, a better understanding of the *in vivo* function of AQP-1 and its connection to cell guidance signaling would be beneficial to studies in cell migration and invasion in cancer and developmental biology.

In this study, we examined the expression and function of AQP-1 during chick cranial neural crest cell migration and possible upstream guidance and downstream AQP-1 effectors. We first characterized *AQP-1* mRNA and AQP-1 protein expression within migrating cranial neural crest cells using three dimensional (3D) confocal and super resolution microscopy. We examined the role of AQP-1 *in vitro* and *in vivo* by measuring changes to the neural crest cell migratory pattern, individual cell behaviors, and filopodial dynamics after gain- and loss-of-function of AQP-1. To test our hypothesis of a 'bulldozer' role for AQP-1-expressing neural crest cells, we analyzed focal adhesion activity, integrin localization and ECM degradation after AQP-1 manipulation. We examined the possible colocalization of Eph guidance receptor expression with AQP-1 in the same migrating neural crest cells using multiplexed fluorescence *in situ* hybridization. Finally, we use computer simulations to predict what AQP-1 related functions are likely to enhance cell migration.

[1]Stowers Institute for Medical Research, Kansas City, MO 64110, USA. [2]University of Oxford, Wolfson Centre for Mathematical Biology, Mathematical Institute, Woodstock Road, Oxford OX2 6GG, UK. [3]Department of Computer Science, Parks Road, Oxford OX1 3QD, UK. [4]Department of Anatomy and Cell Biology, University of Kansas School of Medicine, Kansas City, KS 66160, USA.

*Author for correspondence (pmk@stowers.org)

R.M.L., 0000-0002-0582-3220; M.C.M., 0000-0002-6819-1419; P.M.K., 0000-0001-6354-9904

Received 2 October 2019; Accepted 3 December 2019

Development (2020) 147, dev185231. doi:10.1242/dev.185231

Together, our data demonstrate a crucial role for AQP-1 during cranial neural crest cell migration and offer a mechanistic basis for *in vivo* AQP-1 function to promote cell invasion.

RESULTS

AQP-1 mRNA is expressed in migrating cranial neural crest cells and preferentially higher within the lead subpopulation

To detect the expression of *AQP-1* mRNA *in vivo* specifically within migrating cranial neural crest cells, we took advantage of our recently optimized integrated protocol combining RNAscope multiplexed fluorescence *in situ* hybridization, immunohistochemistry and tissue clearing with FRUIT (Morrison et al., 2017b). This enabled the detection of *AQP-1* mRNA expression in migrating HNK-1-labeled neural crest cells (Fig. 1A-C). By spot counting the number of *AQP-1* transcripts per neural crest cell, we found that *AQP-1* expression was visible in migrating cranial neural crest cells observed at Hamburger and Hamilton stage (HH) 13 (Hamburger and Hamilton, 1951) en route from rhombomere 4 (r4) to the second branchial arch (BA2) (Fig. 1C; neural crest cells are color-coded to show number of *AQP-1* counted transcripts). In a typical r4 neural crest cell migratory stream, the highest numbers of detected transcripts of *AQP-1* were found to be in the cell subpopulation at the front of the migratory stream (Fig. 1C). We determined this by quantifying the fluorescence signal of *AQP-1* mRNA expression as a function of distance along the migratory stream (from the neural tube towards BA2) in a large number of cells/embryos (Fig. 1D). This confirmed that lead neural crest cells showed a significantly higher level of *AQP-1* expression compared to cells further back in the invading stream (Fig. 1D).

AQP-1 protein is localized on the cell membrane of neural crest cells, including filopodia, *in vitro* and is expressed throughout the migratory stream *in vivo*

Whether AQP-1 protein is expressed within subregions of individual migrating neural crest cells is difficult to determine because it is challenging to resolve fluorescence signal in thin (1-2 µm wide) protrusions. Structured illumination microscopy (SIM) has emerged as an excellent tool for resolving diffraction-limited issues by increasing optical resolution (Gustafsson et al., 2008). When we applied SIM to visualize AQP-1 protein location within migrating neural crest cells *in vitro*, we discovered AQP-1 was present on the cell membranes, including the tips of filopodia (Fig. 1E). To determine AQP-1 protein expression *in vivo*, we analyzed AQP-1 protein by immunohistochemistry within HNK-1-labeled migrating neural crest cells and confirmed AQP-1 expression throughout the migratory stream (Fig. 1F,G; HH11-15). Furthermore, by quantifying fluorescence intensity in individual leader and follower neural crest cells, we determined that there is a higher level of AQP-1 protein in the lead neural crest cells *in vivo* (Fig. 1H). These data suggest that AQP-1 may be influencing dynamic cellular shape changes by acting as a water channel at the leading edge of the migratory stream.

AQP-1 perturbations *in vitro* alter neural crest cell speed

To begin to determine the function of AQP-1 in cranial neural crest cell migration, we explanted cranial neural tubes in an *in vitro* assay and measured changes in cell migratory behaviors with confocal time-lapse microscopy (Fig. 2A,B). We took advantage of acetazolamide (AZA), a chemical inhibitor of AQP-1 function (Bin and Shi-Peng, 2011; Zhang et al., 2012; Cai et al., 2018; Ameli et al., 2012). Although AZA can also affect AQP-4 function, AQP-1 is the only aquaporin significantly expressed by the invasive front of the migratory stream and therefore the only aquaporin significantly affected by AZA in this assay (Huber et al., 2007; McLennan et al., 2015a; Morrison et al., 2017a). When we inhibited AQP-1 function *in vitro*, we observed that the migrating neural crest cells moved significantly more slowly than control neural crest cells (in the presence of DMSO) (Fig. 2B,C; Movie 1). Representative tracks

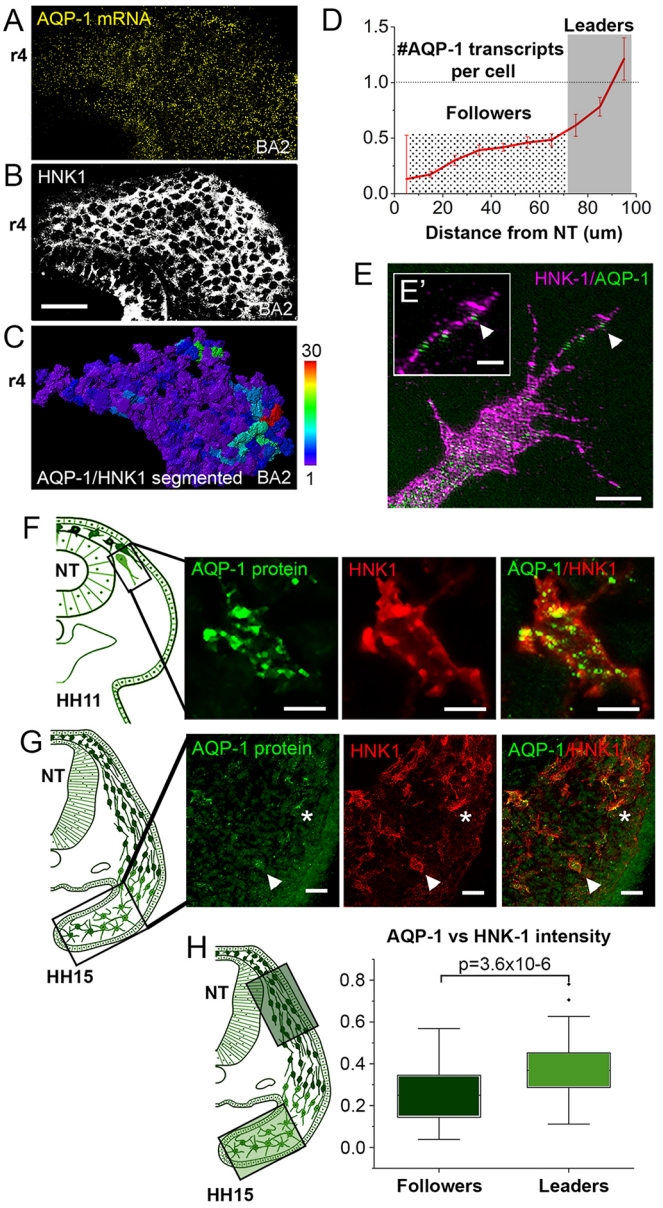

Fig. 1. Aquaporin 1 is expressed by neural crest cells at the invasive front of the migratory stream and is located in filopodia. (A-C) Expression of *AQP-1* mRNA by RNAscope (A) in migrating cranial neural crest cells co-labeled with HNK-1 (B) with the number of *AQP-1* transcripts per neural crest cell counted (C). Scale bar: 30 µm. (D) Quantification of the number of *AQP-1* mRNA transcripts per cell versus distance from the neural tube. *n*=~7500 cells, *n*=10 embryos. Data are mean±s.e.m. (E) High-resolution image of the neural crest cell protrusions *in vitro* showing AQP-1 protein (green) in the filopodia (arrowheads). Scale bars: 5 µm; 2 µm for inset. (F) Schematic representation of transverse section and high-resolution images of migrating neural crest cells (red) at HH11 with AQP-1 protein (green). Scale bars: 10 µm. (G) Schematic representation of transverse section and images of migrating neural crest cells (red) at HH15 with AQP-1 protein (green). AQP-1-rich neural crest is marked with an arrowhead and asterisk. Scale bars: 20 µm. (H) Quantification of the AQP-1 protein intensity versus HNK-1 intensity from transverse cryostat sections; *n*=70 leader cells, *n*=51 follower cells.

Development (2020) 147, dev185231. doi:10.1242/dev.185231

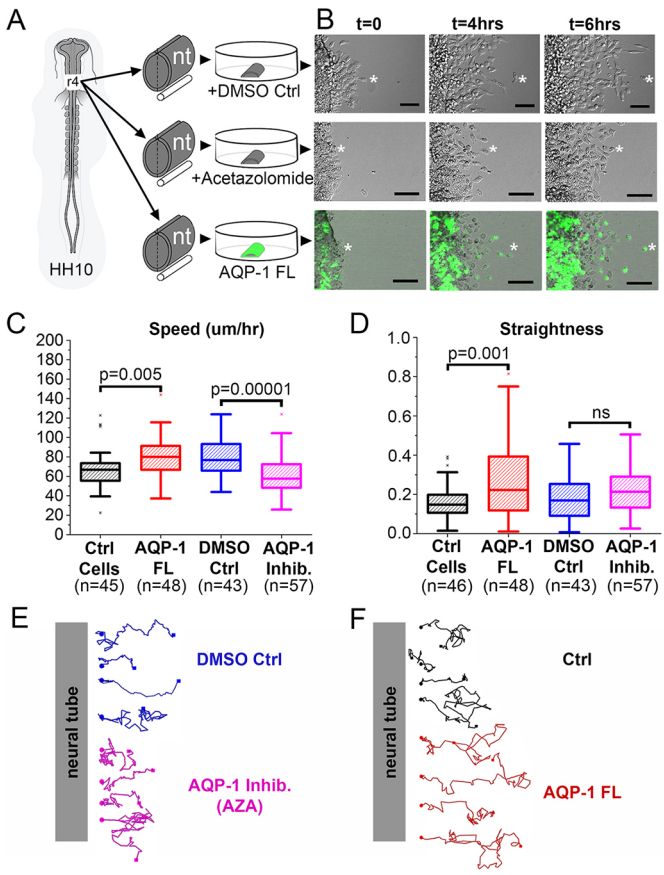

Fig. 2. AQP-1 modifies neural crest cell speed *in vitro*. (A) Schematic representation of experimental setup. (B) Representative images of *in vitro* neural crest cell time-lapses with neural crest cells exposed to DMSO (control for AZA treatment), AZA and transfected with AQP-1 FL. Asterisk indicates the furthest migrating cell. Scale bars: 50 µm. (C) Box plot of the speed (µm/h) of neural crest cells with overexpression of AQP-1 (red, *n*=48 cells from *n*=8 neural tube explants) and corresponding untransfected control cells from the same cultures (black, *n*=45 cells from *n*=6 neural tube explants), and AQP-1 inhibition (pink, *n*=57 cells from *n*=4 neural tube explants) and corresponding DMSO controls (blue, *n*=43 cells from *n*=5 neural tube explants). (D) Box plot of the straightness of neural crest cells with overexpression of AQP-1 (red, *n*=48 cells from *n*=8 neural tube explants) and corresponding untransfected control cells from the same cultures (black, *n*=46 cells from *n*=6 neural tube explants), and AQP-1 inhibition (pink, *n*=57 cells from *n*=4 neural tube explants) and corresponding DMSO controls (blue, *n*=43 cells from *n*=5 neural tube explants). (E) Representative tracks of neural crest cells with AQP-1 inhibition (pink) and corresponding DMSO controls (blue). Start points are marked with circles; end points are marked with squares. (F) Representative tracks of neural crest cells with overexpression of AQP-1 (red) and corresponding controls (black). Start points are marked with circles; end points are marked with squares. nt, neural tube; AZA, acetazolamide; Ctrl, control; t, time; hrs, hours.

show that neural crest cells exposed to AZA remain closer to the neural tube explant and to other cells when compared with controls (Fig. 2E).

To determine changes in cell migration after AQP-1 gain of function, we overexpressed AQP-1 in premigratory neural crest cells [by transfection with AQP-1 full-length construct (FL)] and again explanted neural tubes in culture (Fig. 2A,B). AQP-1 overexpression resulted in neural crest cells that moved significantly faster when compared with non-transfected cells in the same culture (Fig. 2B,C; Movie 1). Neural crest cells overexpressing AQP-1 were also significantly faster when compared with EGFP-only (pMES) transfected cells from different cultures that were prepared and imaged concurrently (Fig. S1D). Typical cell tracks from gain-of-function of AQP-1 experiments confirmed that neural crest cells moved further away from the neural tube explant in the same amount of time (Fig. 2F). Interestingly, when AQP-1 was overexpressed, cells migrated with increased straightness compared with their controls (Fig. 2D). These *in vitro* data suggest that AQP-1 significantly influences the speed at which neural crest cells migrate.

Inhibition of AQP-1 *in vivo* results in fewer neural crest cells invading branchial arch 2

To determine the *in vivo* function of AQP-1, we first knocked down AQP-1 function in premigratory cranial neural crest cells by morpholino (MO) transfection. Similar to *in vitro* experiments, AQP-1 MO-transfected neural crest cells did not travel as far as control MO-transfected neural crest cells (Fig. 3A,C,D). In AQP-1 MO-transfected embryos, we found fewer migrating transfected neural crest cells in BA2 compared with control MO-transfected embryos (Fig. 3B). To further verify the *in vivo* loss of AQP-1 function in neural crest cell migration, we microinjected AZA into the paraxial mesoderm adjacent to r4, prior to neural crest cell exit from the dorsal neural tube. The AZA-injected sides of embryos showed fewer migrating neural crest cells moving into BA2 compared with the control sides of the same embryos (Fig. 3F) and control DMSO-injected embryos, as seen with immunolabeling of neural crest cells using HNK-1 (Fig. 3G). We also measured fewer neural crest cells present in BA2 when injected with AZA, as quantified by the percentage of HNK-1 immunostaining signal in BA2 (Fig. 3E). The furthest distance migrated after AZA injection was the same as control, presumably due to cells escaping AZA, to dilution/degradation of AZA over time or to differences in how AZA affects AQP-1 activity when compared with a morpholino (Fig. S1E). There was no significant difference in HNK-1 immunostaining in the control embryos when comparing the control side to the DMSO-injected side (Fig. S1F). These data suggested that AQP-1 expression, and therefore function, promotes efficient neural crest cell invasion *in vivo*.

Overexpression of AQP-1 *in vivo* enhances neural crest cell invasion

To further investigate the role of AQP-1 in neural crest migration *in vivo*, we overexpressed AQP-1 (via transfection with AQP-1 FL) in premigratory cranial neural crest cells. Overexpression of AQP-1 caused neural crest cells to migrate further than control pMES-EGFP transfected neural crest cells at both 12 h (Fig. 3H,I) and 16 h (Fig. 3J,K) after transfection. Measurements confirmed a significant increase in the distance migrated by AQP-1 FL transfected neural crest cells when compared with pMES transfected neural crest cells analyzed at the same time points (Fig. 3L,M). To determine whether the increased distance migrated when AQP-1 was overexpressed was due to an increase in cell speed, we performed *in vivo* time-lapse confocal imaging of the migratory streams at 5 min intervals after control (Gap43-YFP) and AQP-1 FL transfections (Fig. 3N,O; Movie 2). Cell tracking confirmed that neural crest cells migrated further and faster within the invasive front (front 20% of the migratory stream) when transfected with AQP-1 FL than controls (Fig. 3P,S; Movie 2). Interestingly, when neural crest cells were transfected with AQP-1 FL, they also displayed a decrease in cell directionality when compared with pMES transfected neural crest cells (Fig. 3Q). To indicate whether AQP-1 may be playing a role in delamination, the number of transfected cells was counted at 16 h. Although there were statistically more AQP-1 transfected neural

Development (2020) 147, dev185231. doi:10.1242/dev.185231

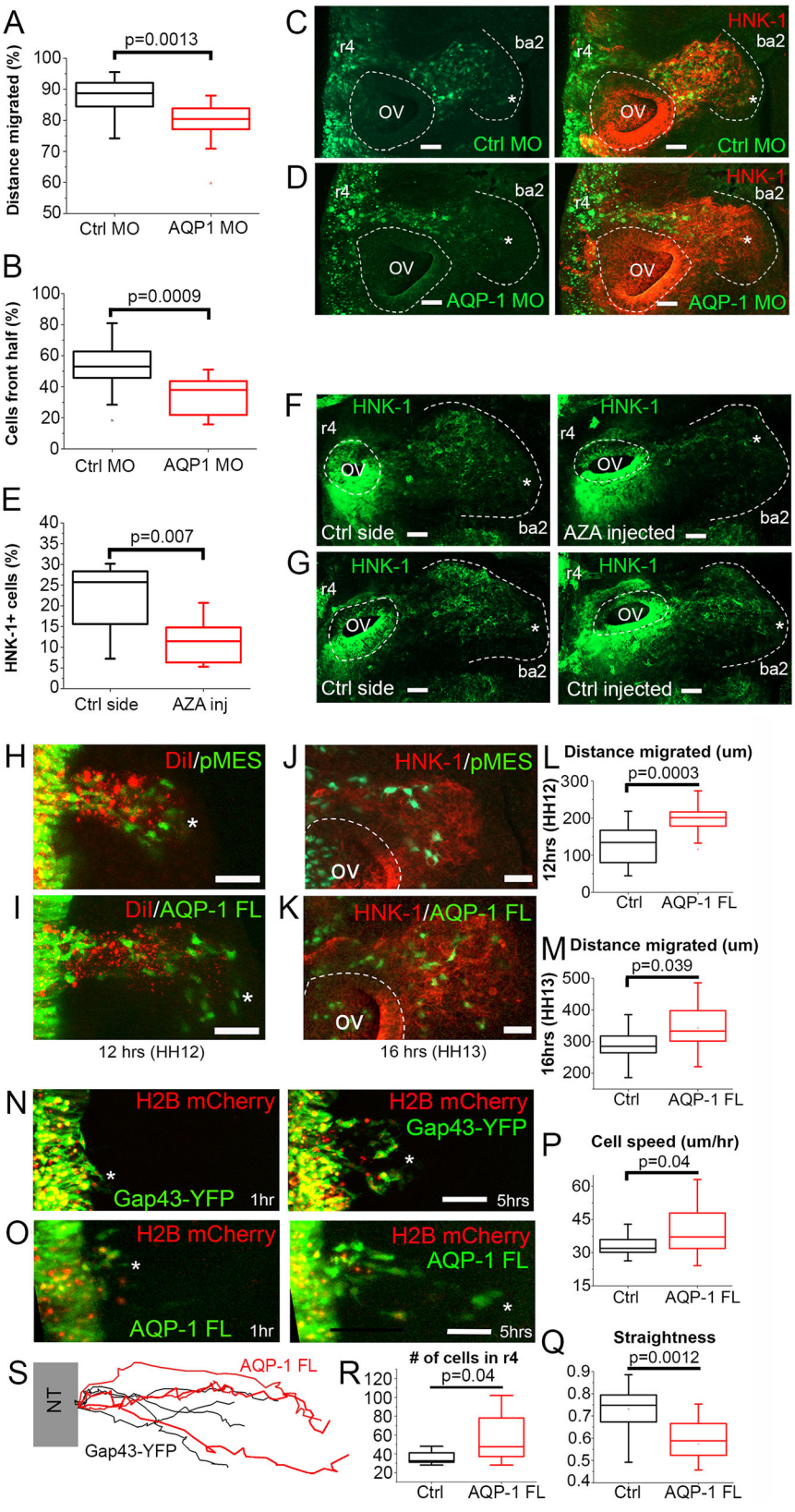

Fig. 3. Neural crest cell migration is decreased when AQP-1 is knocked down and increased when AQP-1 is overexpressed *in vivo*. (A) Box plot of the distance migrated by neural crest cells as a percentage of the whole stream, *n*=15 control MO embryos and 17 AQP-1 MO embryos. (B) Box plot of the percentage area of the branchial arch (front 50% of the stream) containing HNK-1-positive neural crest cells, *n*=15 control MO embryos and 16 AQP-1 MO embryos. (C,D) HH14 embryo in which neural crest cells (red) are transfected with control MO (green) (C) or AQP-1 MO (green) (D). Scale bars: 50 µm. (E) Box plot of the percentage of neural crest cells that migrate into the branchial arches, *n*=6 embryos per treatment. (F,G) HNK-1 labeling of HH15 embryo after injection of AZA (F) or DMSO (G) into the paraxial mesoderm; control and injected sides are shown. Scale bars: 50 µm. (H,I) Neural crest migration 12 h after premigratory neural crest cells were labeled with DiI (red) and transfected with pMES (green, H) or AQP-1 FL (green, I). Asterisk indicates the end of the stream. Scale bars: 50 µm. (J,K) Neural crest migration 16 h after premigratory neural transfection with pMES (green, J) or AQP-1 FL (green, K) and then labeling with HNK-1 (red). Scale bars: 50 µm. (L,M) Box plots of the distance migrated by control (pMES) and AQP-1 FL transfected neural crest cells 12 h (L) and 16 h (M) after transfection. (L) *n*=16 pMES embryos and *n*=15 AQP-1 FL embryos. (M) *n*=11 pMES embryos and *n*=15 AQP-1 FL embryos. (N,O) Selected images from a time-lapse showing neural crest cells migrating into paraxial mesoderm transfected with a nuclear marker (H2B mCherry, red) and Gap43-YFP (green, N) and AQP-1 FL (green, O). Asterisks indicate the most invasive cell. Scale bars: 20 µm. (P) Box plot of the speed of neural crest cells migrating at the front of the stream into paraxial mesoderm; *n*=16 cells for control, *n*=11 cells overexpressing AQP-1. (Q) Box plot of the directionality of the same cells tracked in P. (R) Box plot of the number of transfected cells (pMES and AQP-1 FL) in the neural crest stream 16 h after transfection; *n*=8 pMES embryos, *n*=10 AQP-1 FL embryos. (S) Representative tracks of neural crest cells transfected with Gap43-YFP (black) and AQP-1 FL (red). FL, full length; OV, otic vesicle; ba, branchial arch; AZA, acetazolamide; Ctrl, control; MO, morpholino; r, rhombomere.

crest than pMES, the range of cell numbers varied greatly and may be due to differences in transfection efficiency as opposed to a role in delamination (Fig. 3R). Together, these data suggest that AQP-1 is crucial to the directed neural crest cell invasion but they do not reveal the mechanistic basis underlying this AQP-1 function.

AQP-1 stabilizes neural crest cell filopodia

To begin to address the mechanistic basis of AQP-1 function during cranial neural crest cell migration, we first perturbed AQP-1 function and used spinning disk confocal microscopy on the lead neural crest cells *in vivo* to observe any rapid changes in cell

Development (2020) 147, dev185231. doi:10.1242/dev.185231

morphology and behavior. Specifically, we collected *z*-stacks at 20 to 30 s intervals of neural crest cells transfected with Gap43-mTurquoise2 as well as AQP-1 MO (knockdown), AQP-1 FL (overexpression) or pMES (control) (Fig. 4A,B,J; Movie 3). Images of transfected cells were first processed by creating a binary mask of single cells in ImageJ using the membrane-bound Turquoise2 signal. We then used the CellGeo software (Tsygankov et al., 2014) and additional calculations to identify and measure filopodia length, position, angle and survival time (Fig. 4C-E). With knockdown of AQP-1, we find a significant reduction in the number and length of filopodia in migrating neural crest cells (Fig. 4F,G). In addition, filopodia in cells lacking AQP-1 retracted at significantly faster rates than control cells, leading to less stable filopodia with a shorter survival time (Fig. 4H,I). In contrast, lead neural crest cells in which AQP-1 was overexpressed have enhanced stable filopodia with reduced protrusion and retraction rates, and a longer survival time (Fig. 4H,I). The average number of filopodia per cell was reduced when AQP-1 was overexpressed but their length was unchanged (Fig. 4F,G).

We also examined the direction in which the filopodia extended relative to the direction of migration of the cell. A vector was created from the base of the filopodia to the tip and the angle to the direction of motion was calculated (Fig. S2C). The control filopodia were roughly bi-polar in distribution, pointing both towards and away from the direction of motion, as shown on the rose plot, although the Rayleigh test does indicate a uniform distribution (P=0.2) (Fig. S2A). With overexpression of AQP-1, the filopodia were found to point randomly in all directions (P=0.22) (Fig. S2A). After knockdown of AQP-1 by MO, filopodia on average were directed −60° rostral from the direction of motion roughly towards branchial arch 3 (BA3) (P=4.8×10^{-6}) (Fig. S2A). We considered the possibility that the longest filopodia may be more important for directional migration by comparing the length of the filopodia found in a 30° window around the direction of motion to the length of filopodia in all other directions. For control cells, the filopodia in the direction of migration were significantly longer than the remaining filopodia (P=5.9×10^{-9}) (Fig. S2B). However, this association is lost in both overexpression and knockdown of AQP-1, and the filopodia in the direction of motion are no longer than filopodia elsewhere in the cell (P=0.31 and P=0.2, respectively) (Fig. S2B). These data strongly suggest that AQP-1 functions to stabilize filopodia in migrating neural crest cells; results in the literature suggest that this is likely due to water flux (Papadopoulos et al., 2008; Karlsson et al., 2013; Saadoun et al., 2005).

AQP-1 influences neural crest cell focal adhesions and ECM degradation

To further explore the role of AQP-1 in neural crest cell invasion, we examined whether AQP-1 is involved in two important aspects of cell migration: cell–ECM attachment and ECM degradation. First, we overexpressed AQP-1 in migrating neural crest cells, isolated those cells from developing embryos and performed RNAseq. The sequencing results were compared with those from neural crest cells transfected with pMES only. Significant pathways affected by AQP-1 expression include many guidance signaling pathways, such as semaphorins, FGFs, neuregulin and ephrins, as well as the actin cytoskeleton (Fig. 5A). Members of the AQP family have been shown to promote migration by facilitating the recycling of integrins and therefore the turnover of focal adhesions that are necessary for cell invasion (Chen et al., 2012). When AQP-1 is overexpressed, *integrin A8* and *integrin B5* were significantly increased (Table S1). Therefore, we performed immunohistochemistry for HNK-1,

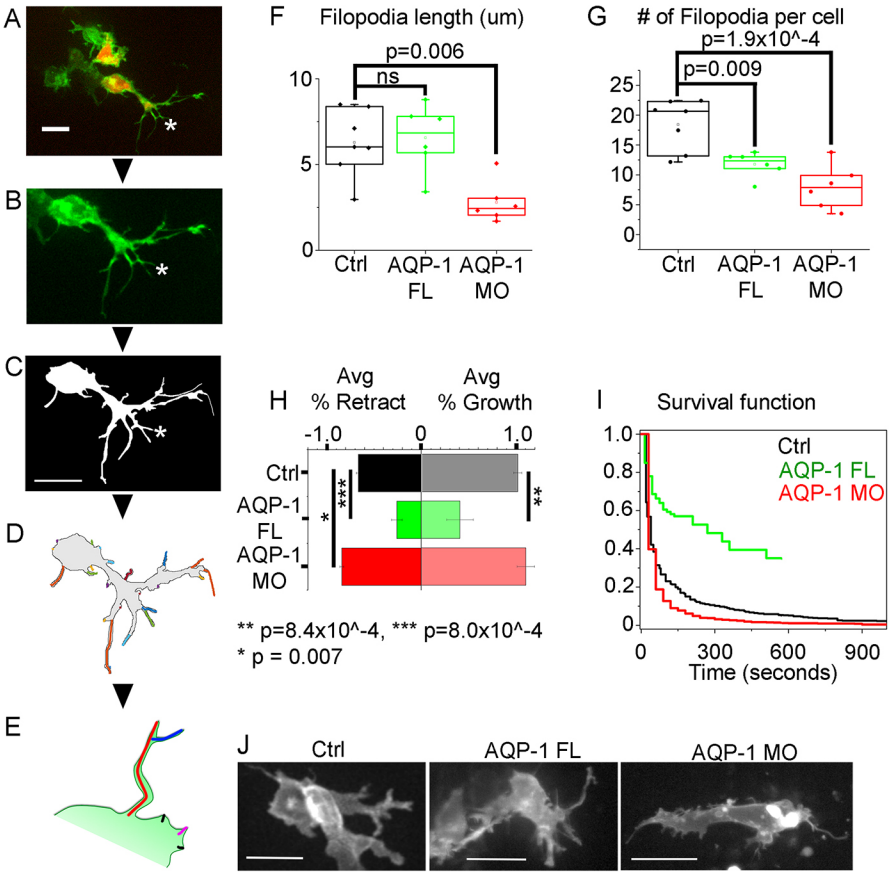

Fig. 4. Identification and tracking of *in vivo* neural crest filopodia reveals AQP-1 expression changes the length, number, growth rate and survival. (A) Front of r4 stream of neural crest cells of a pMES control (red) and Gap43-mTurquoise2 (green)-labeled HH13 embryo. (B) Gap43-mTurquoise2 labeling of individual cells and (C) masked image of a cell for filopodia identification. Asterisks indicate a single filopodia. (D) Each identified filopodium of a single time point for a cell marked in different colors. (E) Schematic of filopodium identification if filopodia are bifurcated; one tip is the main filopodia and the branch constitutes a second filopodium of shorter length. (F) Box plots showing no significant change in filopodia length when AQP-1 is overexpressed, but shorter filopodia when AQP-1 is knocked down by a morpholino. (G) Box plot of the number of filopodia per cell showing a reduction in number if AQP-1 expression is altered. (H) Percentage change in filopodial length from time point to time point for control (pMES), AQP-1 FL and AQP-1 MO cells. AQP-1 overexpression reduces the rate of filopodial growth or retraction but knockdown increases only the retraction rate. (I) Survival function for filopodia under three conditions. The probability of a filopodium in a cell overexpressing AQP-1 is much higher than in control. AQP-1 knockdown reduces the survival probability of a filopodium. (J) Representative Gap43-mTurquoise2 membrane-labeled cells *in vivo*. Scale bars: 20 µm.

Development (2020) 147, dev185231. doi:10.1242/dev.185231

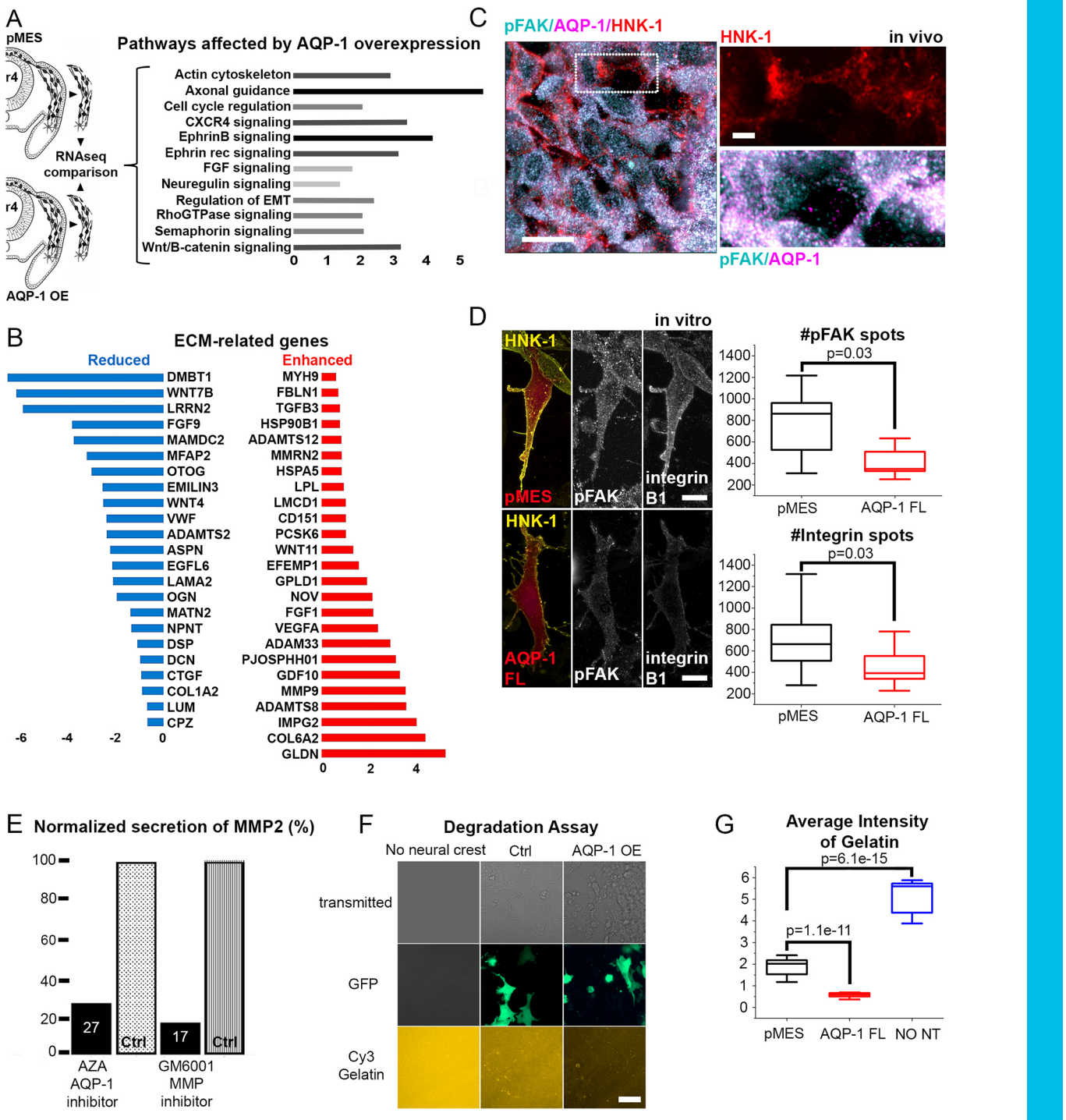

Fig. 5. AQP-1 influences focal adhesions and ECM degradation. (A) Integrated pathway analysis displaying developmentally relevant signaling pathways affected by overexpression of AQP-1. *x*-axis is -log(p-value). (B) Genes associated with an ECM GO term that were significantly up- (red) or downregulated (blue) in response to overexpression of AQP-1. *x*-axis is log2 fold change. (C) Colocalization of pFAK (cyan) and AQP-1 (magenta) protein expression in migrating neural crest cells (HNK-1, red) *in vivo*. Scale bars: 2 µm. (D) High-resolution images of neural crest cells (HNK-1, yellow) *in vitro* transfected with pMES or AQP-1 FL (red) showing pFAK and integrin B1 expression (white). Scale bars: 5 µm. Box plots of the number of pFAK spots (top) and integrin B1 spots (bottom) detected in neural crest cells transfected with pMES or AQP-1 FL, *n*=10 and 12 (top), *n*=10 and 11 (bottom), respectively. (E) Quantification of in-gel zymography using AQP-1 and MMP inhibitors, showing 27% and 17% of MMP activity, respectively; *n*=39 neural tubes each for AZA and control, *n*=32 neural tubes each for GM6001 and control. (F) *In vitro* degradation assay. Chambered slides were coated with Cy3-labeled gelatin (orange). Neural tubes transfected with pMES or AQP-1 FL (GFP) were plated onto the gelatin and incubated for 40 h. No neural tubes were used as baseline control. (G) Box plot of the average intensity of Cy3-labeled gelatin after 40 h of incubation with no neural crest, pMES-transfected neural crest or AQP-1 FL-transfected neural crest; *n*=3 replicates per condition, five random 40× images of each replicate were used in the analysis.

AQP-1 and phosphorylated focal adhesion kinase (pFAK) on cranial neural crest cells in migrating r4 neural crest *in vivo*. Confocal imaging with Airyscan detection revealed a colocalization between the puncta of pFAK and AQP-1 (Pearson's coefficient 0.74), indicating a very close physical proximity of these two proteins (Fig. 5C). To further investigate the possible link of AQP-1

Development (2020) 147, dev185231. doi:10.1242/dev.185231

with pFAK and integrins, we performed immunohistochemistry for HNK-1, pFAK and integrin B1 after transfection with AQP-1 FL (overexpression) or pMES (control) *in vitro*. Using Airyscan confocal microscopy and spot detection analysis, AQP-1 overexpression resulted in fewer pFAK puncta, as well as fewer integrin B1 puncta on or very near neural crest cell membranes. RNAseq analysis showed that integrin B1 RNA levels did not change when AQP-1 was overexpressed (Table S1). Therefore, this result suggests increased turnover of integrin B1 via internalization, which is consistent with previous literature (Chen et al., 2012), or dissociation of the integrin heterodimers as well as internalization or loss of phosphorylation of FAK (Fig. 5D).

From the RNA-seq data, we also focused our attention on the ECM-related genes, as AQP-1, AQP-3 and AQP-4 have all been shown to be positive regulators of the ECM-degrading matrix metalloproteases (MMPs) (Chen et al., 2015; Ding et al., 2011; Jiang et al., 2014; Wei and Dong, 2015; Xiong et al., 2017; Xu et al., 2011). When AQP-1 is overexpressed in migrating neural crest cells, *MMP9* as well as members of the ADAMs, including *ADAM33*, were significantly increased (Fig. 5B). To test whether AQP-1 is upstream of MMP activity, we measured MMP activity from neural crest cells using an in-gel zymography assay. Specifically, neural tube cultures were exposed to either AZA (an AQP-1 inhibitor), GM6001 (MMP inhibitor) or used as controls. The medium from these cultures was then extracted to determine MMP activity. Neural crest cells exposed to AZA exhibited a reduction of MMP activity of 73% at a size that most likely matches MMP2 (Fig. 5E; Fig. S1G). In comparison, neural crest cells exposed to GM6001 exhibited a reduction of MMP activity of 83%, which was our positive control to show that the assay was functional (Fig. 5E; Fig. S1G). This result was verified with an *in vitro* degradation assay, where neural tubes (transfected with AQP-1 FL or pMES) were plated on top of fluorescently labeled gelatin (Garmon et al., 2018). After 40 h of incubation, the assays were imaged, and average fluorescent intensity of the gelatin was quantified as a read out of degradation (Fig. 5F). Neural tubes transfected with pMES significantly degraded gelatin compared with control wells where no neural tubes were plated as expected (Fig. 5F,G). Transfection with AQP-1 FL resulted in even higher gelatin degradation, which is consistent with the in-gel zymography (Fig. 5F,G). These data suggest that AQP-1 is involved in the promotion of integrin turnover and ECM degradation.

AQP-1 expression is colocalized with EphB1 and EphB3 expression in the same migrating cranial neural crest cells

Previous work in commissural axon guidance in mouse has shown evidence for the co-immunoprecipitation of AQP-1 and Eph receptors, namely EphB2, to form a stable complex within a cell (Cowan et al., 2000). As Eph receptors and ephrins are implicated in axon pathfinding, Cowan and colleagues speculated that aquaporins might function in the growth cone to help integrate the guidance information elicited by Eph-ephrin clustering (Cowan et al., 2000). Based on this study, we asked whether the Eph receptors EphB1 and EphB3, previously shown to be highly expressed in the most invasive cranial neural crest cells (McLennan et al., 2015a), were colocalized with AQP-1 in the same migrating cranial neural crest cells. To address this, we used multiplexed fluorescence *in situ* hybridization (RNAscope) to label *AQP-1*, *EphB1* and *EphB3* mRNA expression, and HNK-1 immunohistochemistry to quantify co-expression of these three mRNAs in cranial neural crest cells *in vivo* (Fig. 6A,B). As before, the HNK-1 channel was used to segment r4 neural crest from whole-mount HH13 embryos (white outlines, Fig. 6A,B) and spots of *AQP-1*, *EphB1* and *EphB3* mRNA transcripts were counted per cell. When we quantified the mRNA expression, we found that *AQP-1* mRNA was only found in cells also expressing *EphB1* and/or *EphB3* mRNA although there were many *EphB1*- and/or *EphB3* mRNA-positive cells without *AQP-1* mRNA (Fig. 6C). When we quantified the average number of detected transcripts in migrating neural crest cells, we found that cells expressing *AQP-1* mRNA had a higher number of *EphB1* and *EphB3* mRNA transcripts than their *AQP-1* negative counterparts (Fig. 6D). By immunohistochemistry, we could also verify that AQP-1 protein and EphB1/B3 protein co-label the same neural crest cells *in vivo* (Fig. 6E-H).

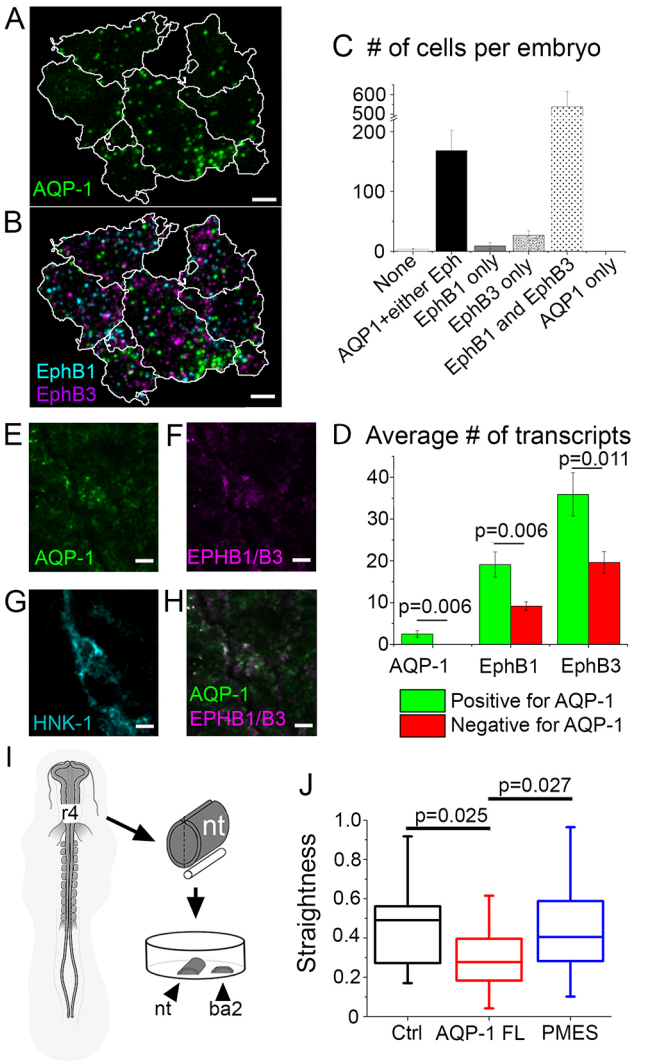

Fig. 6. AQP-1 interacts with EphB receptors and is involved in neural crest cell directionality. (A) RNAscope of lead r4 neural crest cells *in vivo*, HNK-1 signal outlined in white and showing transcripts for *AQP-1* (green). Scale bar: 5 µm. (B) RNAscope of same cells in A with *AQP-1* (green), *EphB1* (cyan) and *EphB3* (purple). (C) Bar graph of number of cells per embryo expressing different mRNA combinations. (D) Bar graph of average number of transcripts of each gene in cells with or without *AQP-1* mRNA. (E-H) Protein expression of AQP-1 (E), EphB1/B3 (F) and HNK-1 (G) in migrating neural crest cells (H) at HH13. Scale bars: 5 µm. (I) Schematic representation of *in vitro* assay quantified in J. (J) Box plot of the directionality of neural crest cells responding to branchial arch 2 tissue *in vitro*; *n*=18 untransfected cells from *n*=4 neural tube explants, *n*=25 AQP-1 FL cells from *n*=5 neural tube explants, *n*=42 pMES cells from *n*=5 neural tube explants.

Development (2020) 147, dev185231. doi:10.1242/dev.185231

AQP-1 is involved in the directed migration of neural crest cells

To explore the hypothesis that AQP-1 is downstream of neural crest cell guidance, we performed *in vitro* cultures where migrating neural crest cells were exposed to BA2 tissue, a known source of guidance signals (Fig. 6I; Movie 4). When AQP-1 was overexpressed in neural crest cells, they were less directed than untransfected controls in the same cultures or in pMES-only transfected neural crest cells (Fig. 6I, J; Movie 4). This finding is consistent with the loss of directionality observed when AQP-1 was overexpressed in neural crest cells *in vivo* (Fig. 3Q) and with the loss of polarized filopodia in the direction of migration (Fig. S2B). One possible explanation for this result is that by overexpressing AQP-1, motility is increased due to more AQP-1 channels, but these channels are no longer focused by complexing with guidance receptors. Overall, these data suggest that AQP-1 is involved in the fast response of cells to guidance factors, possibly by complexing with guidance receptors, including EphB receptors.

Computational modeling predicts that enhanced collective cell invasion is achieved by a combination of increased cell speed, filopodia stabilization and ECM degradation

To test hypothetical mechanistic scenarios by which AQP-1 functions during neural crest cell invasion, we used a hybrid computational model of cranial neural crest invasion. The model consists of a discrete, off-lattice model for the cell dynamics that is coupled to a continuum, reaction-diffusion model of the dynamics of a known cranial neural crest cell chemoattractant (McLennan et al., 2010; VEGF) on a growing domain. The model is based on our previous studies (McLennan et al., 2015a,b, 2012, 2017) and is fully described in the supplementary Materials and Methods. Briefly, we used a two-dimensional approximation of the neural crest cell migratory domain and incorporated finite size effects by considering cells as hard disks that are not allowed to overlap (Table S2; Fig. S3). We used a fixed time step model (with a time step of 1 min) during which a cell senses its environment and moves accordingly. We considered two subpopulations of cells, namely leaders and followers; leaders undertake a biased random walk up a cell-induced gradient of chemoattractant (Table S2).

In this study, we modified five parameters, or features, of our model to simulate the mechanisms by which AQP-1 influences cell migration: cell speed, filopodia stability, filopodia polarity, filopodia number and ECM degradation (Fig. 7A). Filopodia stabilization is realized by a leader sampling the microenvironment only every three time steps and moving persistently in between, as opposed to sampling and potentially moving in a different direction at each time step. Filopodia polarization means that a leader only stabilizes its filopodium when a cell makes an informed movement towards a higher concentration of VEGF as opposed to a random movement. Filopodia number is the number of random directions in which a leader samples the concentration of chemoattractant per time step. As our experimental results showed that overexpression of AQP-1 induced an increase in MMP activity that resulted in ECM degradation (Fig. 5E-G), we introduced into the model the creation of tunnels in the ECM (Fig. 7B). This was implemented by recording the histories of leader positions and defining them as tunnels. Finally, the invasion of cells was assumed to occur on a uniformly growing rectangular domain, the growth of which was based on biological measurements (McLennan et al., 2015a, 2012).

In our computational model (supplementary Materials and methods), we initially quantified changes in the dynamics of cells when we recapitulated the effects of overexpression and downregulation of AQP-1 by modulating relevant model parameters. Different combinations of parameter perturbations are labeled as Model *x* (where *x* can be from 1 to 11); the values of parameters for different models can be found in Fig. 7A. In model simulations, we measured the density of cells along the two-dimensional migratory domain and the likelihood of migratory stream breakage, defined as the proportion of cells not in chains or tunnels at the end of a simulation (Fig. 7D). In the control case, the cell speed was set to 62 µm/h, filopodia were not stabilized and there was a representative number of three filopodia per cell (Model 1). To simulate AQP-1 overexpression, the cell speed was increased by ∼30% to 82 µm/h, filopodia were stabilized and there were two filopodia per cell (Model 2). To simulate inhibition of AQP-1, the cell speed was decreased to 57 µm/h, cells had only a single filopodium, which was not stabilized (Model 3). Initially (Models 1-9), we did not incorporate ECM degradation (i.e. we did not include the tunneling mechanism). For each model, simulations were run ten times with each parameter set, and the results at t=24 h were averaged to account for random variations. As expected, cells at the front traveled farther when their speed was increased (Fig. 7C; Model 2). Cells traveled shorter distances when their speed was reduced to simulate AQP-1 knockdown (Fig. 7C; Model 3). We did, however, observe an unexpected phenomenon; when the cell speed was increased, the simulated cell migratory streams broke apart more frequently and the model did not sustain collective cell migration (Fig. 7D). Migratory stream breakage is not observed *in vivo* and therefore this observation led us to further investigate cell speed versus filopodia dynamics and the effects upon collective cell migration *in silico*.

In our simulations, when cell speed was increased, with or without filopodia stabilization, cells at the front traveled farther compared with the control case (compare Model 4 and Model 5 with Model 1) but stream breakage was much more likely to occur (Fig. 7D,E). The number of filopodia (two or three) affected the likelihood of stream breakage at control cell speeds, with more filopodia resulting in a higher likelihood of breakage but with little impact upon the distance migrated (compare Model 6 with Model 7) (Fig. 7D,E). At higher speeds, whether cells had two or three filopodia did not significantly affect the probability of stream breakage or the distance the cells migrated (compare Model 2 with Model 5) (Fig. 7C-E). Stabilization of filopodia increased the farthest distance traveled by cells regardless of the cell speed. It also noticeably reduced the likelihood of stream breakage at control cell speeds, with a smaller effect at enhanced speeds (compare Model 1 with Model 6, and Model 4 with Model 5) (Fig. 7D,E). Additionally, polarization of filopodia had an insignificant effect on the migration pattern (compare Model 7 with Model 8 and Model 2 with Model 9) (Fig. 7D,F).

As our experimental findings showed that increasing AQP-1 activity led to an increase in MMP activity, and thus to an increase in degradation of the ECM, we included the formation of tunnels by leader cells *in silico*. We found this had no significant effect on distance the cells migrated; however, it did dramatically decrease the percentage of follower cells not in chains to zero (compare Model 1 with Model 10) (Fig. 7D,G). In contrast, to simulate overexpression of AQP-1 in the model and include the effects of increased MMP activity, we increased cell speed, filopodia were stabilized and decreased in number from three to two, and the leaders generated tunnels for the followers. In this scenario, our model predicted that the stream is unlikely to break up and invasion is very robust (compare Model 2 with Model 11) (Fig. 7D,G). Overall, these simulations support the experimental observations that AQP-1 influences cell migration and invasion in multiple ways (Fig. 7H; Movie 5).

Development (2020) 147, dev185231. doi:10.1242/dev.185231

A

	Model #	Speed um/h	Stability filopodia	# of filopodia	tunneling or chain
AQP-1	1	62	No	3	chain
	2	82	Yes	2	chain
reduced ▶	3	57	No	1	chain
	4	82	No	3	chain
	5	82	Yes	3	chain
	6	62	Yes	3	chain
	7	62	Yes	2	chain
	8	62	Yes (polar)	2	chain
	9	82	Yes (polar)	2	chain
	10	62	Yes	2	chain/tun
enhanced ▶	11	82	Yes	2	chain/tun

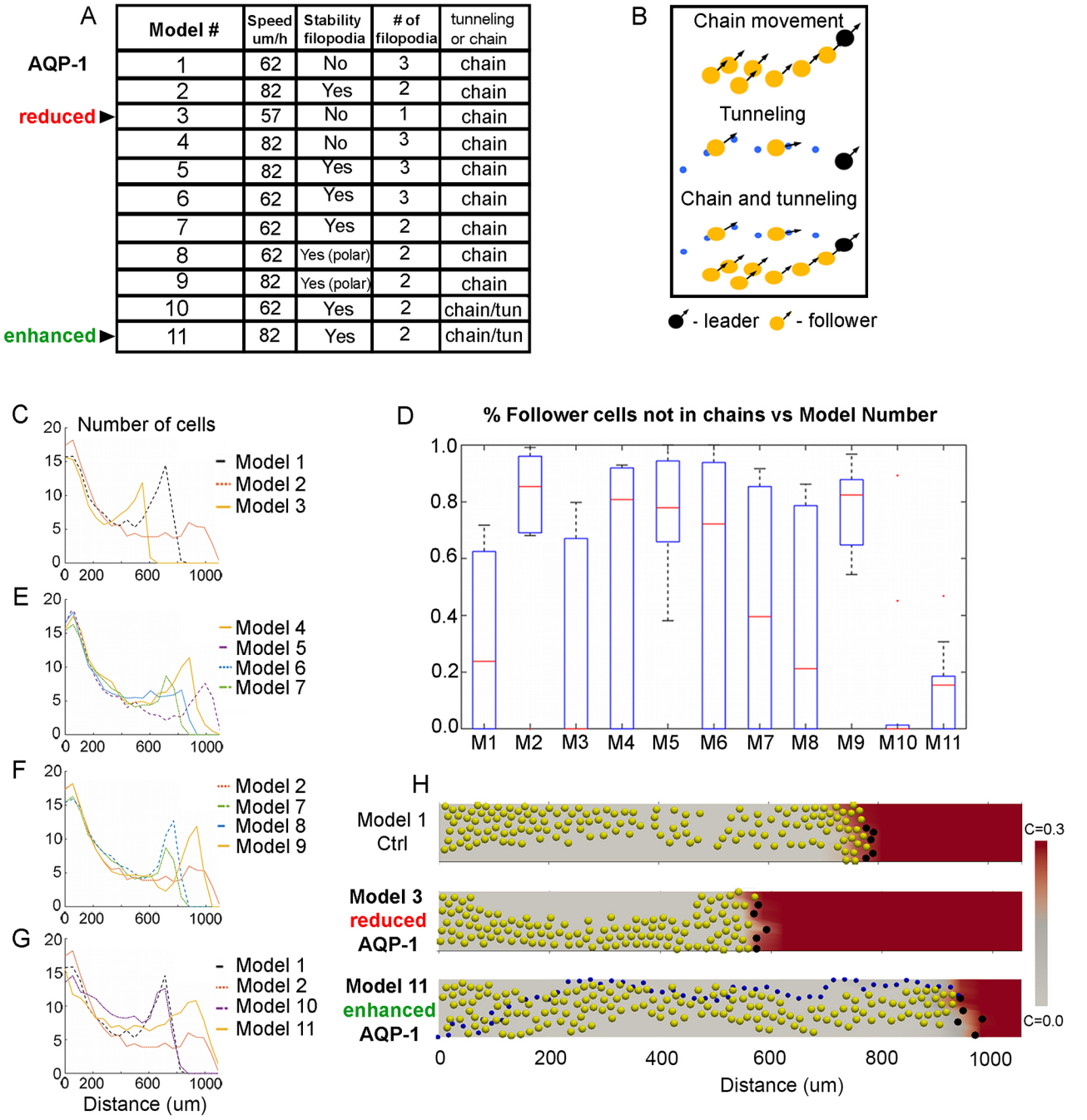

Fig. 7. Computer simulations predict that increased speed, filopodia stabilization and ECM degradation enhance cell invasion. (A) Model parameters for various experimental and hypothetical scenarios. (B) Schematic representations of chain migration where followers (yellow) within a certain distance of each other all adopt the direction of movement of the leader (black), tunnel movement where the tunnel (blue) forged by a leader guides followers that enter the tunnel to move along the tunnel, and a combination of the two. (C,E-G) Distribution of cells along the domain for different models, average of 10 simulations at t=24 h. (D) Box plots of fractions of follower cells not in chains (also not in tunnels in Model 10 and Model 11) at t=24 h. Results are averaged over 10 simulations. For each model, the red line indicates the median, and the bottom and top edges of the box indicate the 25th and 75th percentiles, respectively. The dotted lines extend to the most extreme data points not considered outliers, and the outliers are plotted individually as red dots. M, model. (H) Snapshots from three selected models at t=24 h. Black circles, leader cells; yellow circles, follower cells; blue circles, positions of one of the leaders that form a tunnel; C, concentration of chemoattractant.

DISCUSSION

Our discovery of high AQP-1 expression within lead cells of the chick cranial neural crest cell migratory stream (McLennan et al., 2015a, 2017a) led us to examine the function of this water channel protein. We initially confirmed that *AQP-1* mRNA and protein are both higher in lead cranial neural crest cells *in vivo*, and we used state-of-the-art imaging to show that AQP-1 expression is localized to neural crest cell membranes, including cell filopodia. We tested the hypothesis that AQP-1 regulates cell migration to promote neural crest cell invasion using gain and loss of function of AQP-1, and quantification of cell dynamics obtained from time-lapse imaging sessions. We elucidated four important aspects of AQP-1 function that support its crucial *in vivo* role in neural crest cell migration.

Development (2020) 147, dev185231. doi:10.1242/dev.185231

First, we discovered that modulation of AQP-1 expression altered neural crest cell motility and invasive ability. An increase in AQP-1 expression in premigratory cranial neural crest cells resulted in higher cell speeds *in vitro* and enhanced invasion *in vivo* (Figs 2 and 3). In contrast, the knockdown of AQP-1 function by MO transfection or microinjection of the chemical blocker AZA into the neural crest cell migratory pathway resulted in slower cell speeds *in vitro* and reduced invasion *in vivo* (Figs 2 and 3). These results are consistent with previous data that imply a role for AQP-1 in cell migration and invasion across a wide variety of adult mouse and human cancer cell types (Saadoun et al., 2005; Chen et al., 2012, 2015; Wei and Dong, 2015; Xiong et al., 2017; Cao et al., 2006; Hu and Verkman, 2006; Klebe et al., 2015).

Second, we found that AQP-1 promotes neural crest cell invasive ability by stabilizing filopodia, supporting a function for AQP-1 in enabling cells to 'bulldoze' through the embryonic microenvironment. Initially, we hypothesized that AQP-1 functions to promote neural crest cell invasion by: (1) rapidly changing the cell shape to permit the cell to infiltrate between gaps in loosely connected mesoderm and dense ECM through which cells travel; and/or (2) stabilizing cell filopodia to allow them to break down and displace the surrounding tissue. In support of (2), we found a significant reduction in the number and length of neural crest cell filopodia after AQP-1 knockdown (Fig. 4). Furthermore, neural crest cell filopodia retract faster and survive for shorter durations in cells with reduced AQP-1 function (Fig. 4).

We did not observe overall cell volume changes in migrating neural crest cells *in vivo* by dynamic analysis of three-dimensional cell volumes measured from time-lapse imaging sessions (data not shown). Given that changes in cell size that are induced by alterations in external osmolarity have been linked to AQP-1 function in human vascular smooth muscle cells in culture (Shanahan et al., 1999), we cannot completely rule cell volume changes out because detecting changes in the dynamic filopodia volume of migrating neural crest cells may require higher resolution microscopy. Furthermore, a similar volume of water may flow into or out of control and AQP-1-perturbed neural crest cells, as perturbations are not localized to distinct regions of individual cells.

Third, we learned that AQP-1 directly influences neural crest cell adhesion and ECM degradation, suggesting a mechanistic basis for neural crest cell 'bulldozing' through the microenvironment. In support of this, we showed that AQP-1 and pFAK are colocalized in migrating neural crest cells, and upon AQP-1 overexpression, fewer pFAK and integrin B1 puncta are present on cell surfaces (Fig. 5). This implicates AQP-1 in the integrin-mediated focal adhesion signaling pathways previously shown to be important for neural crest cell migration (Desban and Duband, 1997; Desban et al., 2006; Parsons, 2003). Furthermore, it has been previously shown that AQP-1 regulates FAK expression in bone marrow mesenchymal stem cells (Meng et al., 2014). FAK binds directly to integrin B1, and AQP-2 has been shown to internalize integrin B1 (Chen et al., 2012; Lechertier and Hodivala-Dilke, 2012). Therefore, in migrating neural crest cells, less integrin B1 and pFAK on cell surfaces when AQP-1 is overexpressed may indicate increased integrin turnover and less cell adhesion (Fig. 5). AQP-1 perturbation affects the expression and activity of MMPs in migrating cranial neural crest cells when measured by RNA-seq profiling, in-gel zymography and a degradation assay (Fig. 5). Whether pFAK colocalization with AQP-1 in migrating neural crest cells also plays a role in initiating downstream intracellular signals, including Eph-ephrins, is unclear (Carter et al., 2002; Miao et al., 2000) and will be the focus of future studies. Together, these data clearly demonstrate that AQP-1 promotes neural crest cell invasion by influencing FAK activity, integrin turnover and ECM degradation.

Fourth, we showed that AQP-1 is involved in directed neural crest cell migration, suggesting that AQP-1 is downstream of the ability of a cell to readout guidance factors in the local microenvironment. AQP-1 and EphB receptors have previously been shown to be in the invasive front of the neural crest migratory stream (McLennan et al., 2015a), and here we show that they colocalize in the same migrating neural crest cells at both the RNA and protein levels (Fig. 6). Neural crest cell directionality in response to endogenous guidance cues is reduced when AQP-1 is overexpressed both *in vitro* and *in vivo*, as presumably the majority of the AQP-1 water channels are no longer downstream of guidance signals (Figs 3 and 6). Furthermore, AQP-1 overexpression led to neural crest cell filopodia extending in random directions (Fig. S2). It is not clear whether AQP-1 is enriched in a directional manner, because although there is higher AQP-1 protein expression in lead migrating neural crest cells *in vivo* (Fig. 1H), our super-resolution microscopy that revealed AQP-1 protein expression in neural crest cell filopodia was performed *in vitro* in the absence of endogenous guidance cues (Fig. 1E). Future experiments that dissect the AQP-1 and EphB signaling relationship and explore other guidance receptors we have previously identified by profiling migrating cranial neural crest cells (McLennan et al., 2015a,b) will help to shed light on this.

Last, in support of AQP-1 function, our computational model simulations identified cell speed, filopodia stabilization and ECM degradation as key parameters for controlling neural crest cell invasion (Fig. 7). When we increase or decrease cell speed to simulate AQP-1 gain or loss of function, respectively, we observe the intuitive changes in the maximum distance traveled by cells (Fig. 7; Models 2, 3; Movie 5). However, unexpected breakdown of the cell migratory stream occurs in silico when the cell speed is increased; a pattern that is not observed *in vivo* (Fig. 3). Examination of cell speed versus filopodial dynamics revealed that stabilization of filopodia rather than filopodia number or polarity increased the furthest distance traveled by cells (regardless of speed) and reduced the likelihood of stream separation (Fig. 7). Thus, our computational model simulations support a role for AQP-1 in promoting neural crest cell invasion through ECM degradation, stabilization of filopodia and regulation of cell speed.

In summary, our findings implicate four AQP-1-related processes in neural crest cell migration: modulation of cell speed, stabilization of filopodia, cell adhesion and ECM degradation, and co-localization with cell guidance receptors (Fig. 8). Whether these functions are dependent or independent of AQP-1 functioning as a water channel is currently unknown; however, given the vast recent literature on AQP-1 it is likely to be related to its water transport functions. By stabilizing filopodia, increasing MMP-mediated ECM degradation and controlling adhesions in response to guidance receptors, lead neural crest cells 'bulldoze' through the embryonic microenvironment in a directed manner (Fig. 8). Later-emerging neural crest cells are able to follow and collective migration is maintained. Computational modeling has identified cell speed, filopodia stabilization and ECM degradation as key parameters for promoting neural crest cell migration. The combination of computational modeling with an *in vivo* dynamic imaging platform with single cell resolution provides a powerful tool with which to examine both the upstream regulation of AQP-1 activity and the downstream signaling events in directed cell migration. With the established high correlation of AQP-1 expression and cancer cell aggressiveness (Tomita et al., 2017; De leso and Yool, 2018), our data relating to *in vivo* AQP-1 function during embryonic neural crest cell migration and the

Development (2020) 147, dev185231. doi:10.1242/dev.185231

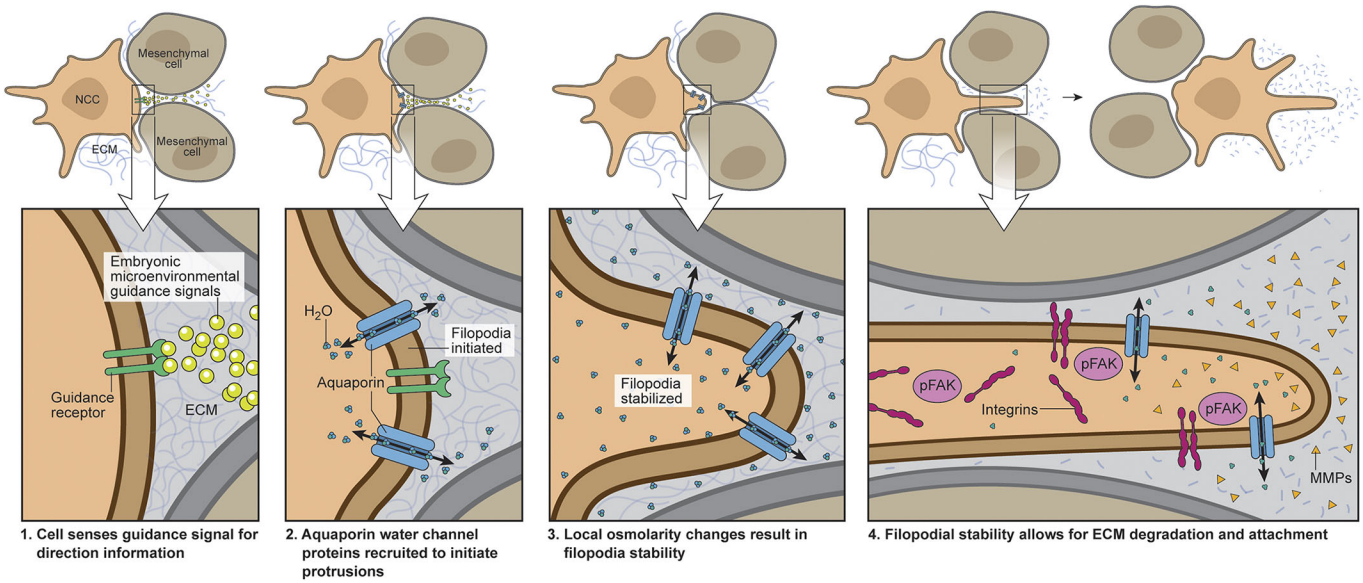

Fig. 8. Schematic representation of the role of AQP-1 in neural crest cell invasion. Neural crest migration is directed by sensing guidance factors in the surrounding microenvironments through which they travel. AQP-1 channels are then recruited by the guidance receptors to initiate protrusive activity in the direction of migration. The AQP-1 channels stabilize the filopodia as well as increase focal adhesion turnover and MMP-mediated ECM degradation. These mechanisms allow neural crest cells at the front of the migratory stream to bulldoze through the microenvironments they encounter.

mechanistic basis of cell bulldozing offer further details on, and illustrate the importance of, the function of aquaporins in development and cancer.

MATERIALS AND METHODS

Embryos

White Leghorn, fertilized chicken eggs (Centurion Poultry, Lexington, GA, USA) were incubated in a humidified incubator at 38°C to the desired developmental stage (Hamburger and Hamilton, 1951).

RNAscope and immunohistochemistry

RNAscope on whole chick heads was performed as previously described (Morrison et al., 2017b). Briefly, HH13 chick embryos were harvested and fixed in 4% paraformaldehyde for 2 h. Following a dehydration gradient of methanol, embryos were stored for 4 days at −20°C before the RNAscope protocol began. After rehydration, embryos were digested in a 0.1× dilution of protease solution in PBS-Tween for 6 min at 22°C with gentle agitation. AQP-1, EphB1 and EphB3 RNAscope probes were designed by Advanced Cell Diagnostics against the relevant gene (GenBank Accession Numbers NM_001039453.1, NM_205035.1 and XM_422762.4, respectively). AQP-1 was labeled with Cy3, EphB1 with Atto488, and EphB3 was labeled with Cy5 dyes. As a control, embryos were processed as described but no probes were used (Fig. S1A). After RNAscope, immunohistochemistry was performed with a 4% molecular biology-grade BSA blocking buffer using HNK-1 primary antibody (TIB-200 hybridoma cell line, ATCC Cell Lines) at a 1:25 concentration (overnight incubation at 4°C). Secondary antibody Alexa Fluor 594 goat anti-mouse IgM (A21044, ThermoFisher Scientific) was used at 1:500 overnight at 4°C. The embryos were then cleared with FRUIT clearing buffer (Hou et al., 2015) at 60% followed by 80% overnight at 4°C.

Immunohistochemistry on cryosections or whole-mount chick heads was performed with either anti-Phospho-FAK (Tyr861) (44-626G, ThermoFisher Scientific) at 1:200, anti-AQP-1 (Millipore, AB3272) at 1:50 or anti-EphB1/3 (sc-926, discontinued product, Santa Cruz Biotechnology) at 1:100. Generally, tissue was fixed in 4% PFA overnight at 4°C. After washing in PBS, tissue was blocked with 4% BSA, 0.1% Tween block for 2 h at room temperature followed by overnight incubation with primary antibodies at 4°C. After washing in 0.1% Tween block, secondary antibodies were applied at 1:500 overnight at 4°C. After a final wash with PBS, whole heads were mounted for imaging and cryosections were coverslipped using Vectashield HardSet Antifade Mounting Medium with DAPI (H-1500, Vector Laboratories). The *z* stacks of the collected images were loaded into Imaris 9.20. The images were segmented using the surface function with HNK-1 setting (settings: grain size at least 0.439 µm, largest sphere 1.65 µm, threshold automatically detected at upper end, lower end 110, estimated diameter 6-7 µm, voxels above 1000). Cells were then selected at the back and front, respectively, of the r4 stream. The mean intensity of the HNK-1 was recorded. The HNK-1 intensity value was normalized from a spot detected outside the cells on the same slide to account for background. The cell intensity was averaged and plotted on a box plot via Origin for the front and the back of the stream.

Secondary antibodies used were: goat anti-rabbit IgG (H+L) (CM405F, Biotium) for pFAK, F(ab')2-goat anti-rabbit IgG (H+L) Cross-Adsorbed Secondary Antibody, Alexa Fluor 546 (A-11071, ThermoFisher Scientific) for AQP-1, Alexa Fluor 488 goat anti-rabbit 488 (A-11008, ThermoFisher Scientific) for EphB1/3 and Alexa Fluor 647 goat anti-mouse IgM (A-21238, discontinued product, ThermoFisher Scientific) for HNK-1. All secondary antibodies were used at 1:500.

Pearson's coefficients for colocalized fluorescence were calculated in Imaris 9.0.0 using the Coloc module on 3D datasets. Images of pFAK, HNK-1 and AQP-1 immunohistochemistry from different regions of the r4 migratory neural crest stream were created using a 40×1.2NA objective with Airyscan imaging on a LSM 800 (Zeiss), with the exception of Fig. 1E, which was acquired on a DeltaVision OMX structured Illumination microscope (GE Lifesciences) with a 60×1.4NA objective. Post-Airyscan processing, a mask was created with the HNK-1 channel to isolate neural crest and thresholds for pFAK and AQP-1 channels were created to eliminate background. Pearson's coefficient for n=5 embryos was recorded and averaged.

In vitro assays

In vitro neural tube cultures were performed as previously described (McLennan et al., 2010) using Ham's F-12 Nutrient Mix media (11765054, ThermoFisher Scientific). For the initial experiments to examine cell speed, DMSO was added to the media for controls for the AZA (A6011, Sigma-Aldrich) experiments because AZA was solubilized in DMSO. To transfect some cells in the neural tube cultures with AQP-1 FL, dorsal neural tubes were electroporated *in ovo* as previously described (McLennan and Kulesa, 2007) and allowed to recover for 2-4 h before being removed and plated

Development (2020) 147, dev185231. doi:10.1242/dev.185231

in vitro. Alternatively, neural tubes were removed from embryos and then constructs or morpholinos were electroporated into the tissue using petri dish platinum electrode for tissue chamber (45-0505, BTX), 5 pulses, 60 V. Neural tubes were allowed to recover in the chamber for 10 min and were then plated. The AQP-1 FL construct was designed and built in the lab, using pMES as a backbone. Prior to neural crest experiments, AQP-1 FL was tested in a chick cell line and shown to overexpress AQP-1 (Fig. S1B,C). For the directionality towards the BA2 tissue experiments, neural tubes were soaked in Hoechst (1:200 dilution for 5 min prior to plating) and BA2 tissue was soaked in DiI (V22889, ThermoFisher Scientific) (1:30 dilution for 30 min). Time-lapses of cultures were taken on a LSM 710, LSM 780 or LSM 800 (Zeiss) at 2.5 min intervals (single z-planes). For immunohistochemistry on *in vitro* cultures, the same antibodies and protocols were followed as for cryosections and whole-mount embryos; however, the incubation times were shorter. *In vitro* cultures were fixed with 4% paraformaldehyde for 20 min. Cultures were incubated with primary and secondary antibodies for 1 h each. Images were taken using confocal microscopy and Airyscan detection with a 40×1.2NA water immersion objective. Owing to the length of time taken to collect Airyscan *z* stacks and to reduce possible photobleaching, this imaging was not performed for the entire cell but focused on the cell membranes against the fibronectin-coated dish surface.

The *z* stacks of the collected images were loaded into Imaris 9.20. The cells were segmented using the surface function to manually outline the shape of the cell. Spots were then detected on each integrin and pFAK channel. The integrin channel spots included a diameter of 0.6 µm spot with background subtraction and a quality filter was picked using a statistical upper and lower threshold break in the data. The pFAK spots were detected using 0.4 µm spots, and background subtraction with the quality filter was picked using a statistical upper and lower threshold break in the data. The number of spots for each cell was recorded for pFAK and integrin channels, then an average was calculated for each data set. The data were then plotted on a box plot via Origin.

For the neural tube cultures with DMSO, AZA or AQP-1 FL, cells were manually tracked using 'Spot' detection in Imaris for ≥6 h. The spots were set to ≥9 µm in size. The mean speed and displacement of each track was calculated using Imaris (Bitplane). Straightness equals displacement of track divided by length of track. The box plots in each figure were generated by using the values from each dataset indicated. Boxes and whiskers indicate the quartiles (25-75%) and range (minimum to maximum values apart from outliers as determined by the software), respectively, of each dataset. *P*-values were calculated using a standard Student's *t*-test or paired *t*-test. Data distribution was assumed to be normal, but this was not formally tested.

In ovo injections, electroporations and analysis

AZA (500 µM) was injected into multiple sites of the mesoderm on one side adjacent to the hindbrain region of HH8-9 embryos. For control injections, the same injections were performed using DMSO. After 24 h reincubation, embryos were fixed in 4% paraformaldehyde for 2 h at room temperature and then immunohistochemistry was performed for HNK-1 as described above. Each cranial region of injected embryos was then cut down the midline and each half mounted in a glass slide as previously described (Teddy and Kulesa, 2004). Both halves of the cranial region of each embryo were imaged on a LSM 800 (Zeiss) so that injected and control halves of each embryo could be compared. *In ovo* electroporations were performed as previously described (McLennan and Kulesa, 2007). Fluorescein-tagged AQP-1 and control morpholinos were designed by, and obtained from, Gene Tools. H2B mCherry (2.5 µg/µl) and morpholinos (0.5 mM) were injected and electroporated at HH8-9 and reincubated for 20 h before being fixed, processed for HNK-1 and imaged as described above. An empty EGFP vector, pMES, was used as a control for AQP-1 FL, as AQP-1 FL was inserted into the pMES vector. pMES and AQP-1 FL were either injected and electroporated with DiI before being reincubated for 12 h or injected and electroporated without DiI before being reincubated for 16 h. Time-lapses were performed as previously described (McKinney et al., 2013). We calculated the percentage of area covered using the 'Surfaces' function of Imaris (Bitplane) to create a surface mask by manually drawing the outline of the whole branchial arch. Next, we calculated the area of the HNK-1 fluorescence signal using the masked arch surface. We set a consistent intensity threshold to the same value for each dataset, a surface grain size of 1 µm was set, the diameter of the largest sphere was set to 1 µm and then the automatic 'Surfaces' function was applied. We calculated the percentage of the front of arch the HNK-1 signal covered by comparing the two values in the front 50% of the stream. For electroporated embryos, cells were automatically detected using the 'Spot' function in Imaris. The spots were set to ≥9 µm in size. The spots were counted in the front 50% of the stream. The percentage of total spots versus cells in the whole stream was calculated. The percentage of distance the cells migrated was calculated by measuring the total distance of the migratory route and measuring what distance the transfected cells migrated. This was calculated on 3D *z*-stacks using the measurement tool in Imaris. The box plots in each figure were generated by using the values from each dataset indicated. Crosses indicate outliers; boxes and whiskers indicate the quartiles and range, respectively, of each dataset. *P*-values were calculated using a standard Student's *t*-test or paired *t*-test. Data distribution was assumed to be normal, but this was not formally tested.

Spinning disk imaging and analysis

Premigratory neural crest cells were transfected with pMES, AQP-1 FL or AQP-1 MO via *in ovo* electroporation as described above. All perturbations were co-transfected with Gap43-mTurquoise for visualization of membrane dynamics. HH13 chick embryos were mounted dorsal side down on glass-bottomed dishes with a grease-sealed Teflon membrane over the top to preserve humidity (Rupp and Kulesa, 2007). Samples were placed inside a heated chamber around a spinning disk confocal microscope (PerkinElmer, Ultraview), allowed to acclimate to the chamber, and two-channel imaging proceeded until any sign of phototoxicity was observed. Cells in the front 10% of the migratory r4 neural crest stream were chosen for imaging. Images were collected with a 40×1.2NA water immersion objective in 1 µm *z*-steps for up to 15 µm total depth in either 20 or 30 s increments. Time-lapse data were analyzed using a combination of Imaris (Bitplane AG) and ImageJ. If cells were overlapped in *z*, Imaris 3D imaging was used to create a mask of the cell of interest which was then projected onto 2D. A projected image of the cell was imported into ImageJ and after smoothing and background subtraction, an 8-bit binary mask was created using the Gap-mTurquoise2 fluorescence. Minor adjustments to the mask were made by hand for extremely thin filopodia or touching cells. The time-lapse masked image was imported into a modified version of the CellGeo software (Tsygankov et al., 2014) that did not use the java-enabled GUI but allowed for parameter adjustment using the same algorithms. BisectoGraph and FiloTrak modules were used and parameters of 20 smooth, 1 CrR, 1 CutOff, 9 critical length and 5.5 critical width were used. Filopodia were tracked manually. The remainder of the analysis was written in MATLAB (Mathworks) to collect filopodia data from multiple cells under each condition. A total of seven cells from four embryos were used in control, six cells from four embryos for AQP-1-FL, and six cells from three embryos for AQP-1 MO experiments. Statistical significance was determined using an ANOVA with Tukey's HSD post-hoc calculation and *P*-values reported.

Cytometry, RNA-seq and analysis

Premigratory neural crest were electroporated with either AQP-1 FL or pMES and eggs re-incubated for 24 h. The neural crest stream adjacent to rhombomere 4 was isolated from healthy ∼HH15 embryos. Five pMES transfected embryos were pooled for each of the three biological replicates (n=15 total). Four AQP-1 FL embryos were pooled for each of the three biological replicates (n=12 total). Tissue was dissociated as previously described (McLennan et al., 2015a). Cells were isolated by FACS, which included forward scatter, side scatter, pulse width, live/dead stain (7AAD) and YFP gates, as previously described (McLennan et al., 2015a; Morrison et al., 2017a). Cells were sorted directly into 7 µl of Clontech lysis solution containing 0.05% RNAse inhibitor. Following lysis for 5 min at room temperature, lysates were immediately frozen on dry ice and stored at −80°C. Bulk RNA-seq lysates were thawed on ice. cDNA synthesis and library preparation were performed with SMART-seq v4 Ultra Low Input RNA-seq (634891, Takara, Kusatsu) and Nextera XT DNA sample prep and indexing library preparation kits, as recommended by the manufacturer (FC-131-2001, FC-131-2004 and FC-131-1096, Illumina). Resulting short fragment libraries

Development (2020) 147, dev185231. doi:10.1242/dev.185231

were checked for quality and quantity using a Bioanalyzer (Agilent) and Qubit Fluorometer (Life Technologies). Libraries were pooled, re-quantified and sequenced as 50 bp single reads on two lanes of the Illumina HiSeq 2500 in High Output mode using HiSeq Control Software v2.2.58 (Illumina). Following sequencing, Illumina Primary Analysis version RTA v1.18.64 and bcl2fastq2 v2.18 were run to demultiplex reads for all libraries and generate FASTQ files. More than 3 million total alignments were produced per sample. Single-end 51-base reads were aligned to the chicken genome galGal4 from UCSC with annotations from Ensembl 84 using STAR (2.5.2b) with options –alignEndsType EndToEnd and sjdbScore 2. Downstream analysis was carried out in R (3.4.1). Differential expression analysis was performed using the edgeR package (3.18.1). Genes were indicated as differentially expressed if they had a *P*-value less than 0.05 and a fold change greater than 1.5-fold (absolute value). Gene ontology enrichment was carried out using a hypergeometric test on lists of differentially expressed genes.

In-gel zymography

To achieve high levels of MMP secretion from neural crest cells grown in culture, neural tubes were isolated, plated onto the bottom of four-well dishes (176740, ThermoFisher Scientific) with no coating and covered in 250 µl of Ham's F-12 media. Thirty-nine neural tubes were exposed to 100 µM AZA, 39 neural tubes were exposed to DMSO (0.05 µl in 1 ml) as control for AZA, 32 neural tubes were exposed to 50 µmol/l GM6001 (Anderson et al., 2006) and 32 neural tubes were exposed to DMSO (1 µl in 1 ml) as control for GM6001. After 24 h of incubation, the media were harvested. Protein in media was concentrated using 3K Pierce concentrator (88512, ThermoFisher Scientific) and then used in-gel zymography following the supplier's protocol (ZY00100BOX, LC2670, LC2671, LC2675, LC2676, ThermoFisher Scientific). The substrate was gelatin. Importantly, an image of the gel prior to colloidal blue staining (LC6025, ThermoFisher Scientific) was taken so that the protein ladder could be clearly seen for determining protein size after staining. Quantification of the bands on the gel image were performed using ImageJ and a protocol from Protocol Place (protocol-place.com/assays/gelatin-zymography/).

Degradation assay

A degradation assay was performed using QCM Gelatin Invadopodia Assay (ECM671, Millipore). Cy3-labeled gelatin-coated wells in 8-well chambered slides (80821, Ibidi) were used. The protocol was slightly modified by heating all the gelatin to 60°C so that there was no issue with room temperature and warm gelatin not mixing fully. To optimize cell adhesion, fibronectin was then added over the gelatin as previously described (Garmon et al., 2018). Fifteen neural tubes (transfected with either pMES or AQP-1 FL) were plated into each well with 500 µl of media and incubated for 40 h. For controls, some wells received no neural tubes, but were still incubated for 40 h with 500 µl of media. Cultures were fixed with 4% paraformaldehyde for 20 min and then imaged. MMP2 and MMP9 are secreted proteases and possible gelatin degradation will occur throughout each well, not just where neural crest cells are migrating. Therefore, Cy3-labeled gelatin was imaged at five randomly chosen areas of each well using a 40×1.2NA objective, n=3 wells per condition. The z-stack images were loaded into Imaris 9.20. A surface rendering was created on the whole Cy3 gelatin channel throughout the whole image with the automatic settings used to detect the surface using voxel totals above 10. The average intensity across the whole image for the Cy3 channel was recorded. An average was taken from each condition and a box plot was made using Origin.

Acknowledgements

We thank members of the Microscopy, Histology and Molecular Biology core facilities, and our Scientific Illustrator, Mark Miller, at the Stowers Institute for Medical Research.

Competing interests

The authors declare no competing or financial interests.

Author contributions

Conceptualization: R.M., D.A.R., C.A.M., P.M.K.; Methodology: R.M., M.C.M., J.C.K.-K., D.A.R., C.A.M., R.G., M.R., R.E.B., P.K.M.; Software: M.C.M., J.M.T.; Validation: R.M., M.C.M., P.K.M.; Formal analysis: M.C.M., J.M.T., J.A.M., R.E.B., P.K.M.; Investigation: R.M., M.C.M., J.A.M., J.C.K.-K., D.A.R., C.A.M., R.G., R.E.B., P.M.K.; Resources: R.M.; Data curation: M.C.M., J.M.T., J.A.M., J.C.K.-K., D.A.R., R.G., M.R.; Writing - original draft: R.M., M.C.M., R.G., R.E.B., P.K.M., P.M.K.; Writing - review & editing: R.M., M.C.M., J.M.T., R.G., R.E.B., P.K.M., P.M.K.; Visualization: R.M., M.C.M., J.M.T., J.A.M., R.G., M.R., P.K.M., P.M.K.; Supervision: R.M., M.R., R.E.B., P.K.M., P.M.K.; Project administration: R.E.B., P.K.M., P.M.K.; Funding acquisition: R.G., M.R., P.K.M., P.M.K.

Funding

P.M.K. acknowledges kind and generous funding from the Stowers Institute for Medical Research. R.G. gratefully acknowledges funding from the Engineering and Physical Sciences Research Council (EP/G03706X/1). M.R. gratefully acknowledges research support from the Engineering and Physical Sciences Research Council Cross-Disciplinary Interface Programme (EP/I017909/1). R.E.B. is a Royal Society Wolfson Research Merit Award holder and a Leverhulme Research Fellow.

Data availability

The data from this publication have been deposited in GEO under accession number GSE121131.Original data underlying this manuscript can be accessed from the Stowers Original Data Repository at www.stowers.org/research/publications/libpb-1397.

Supplementary information

Supplementary information available online at http://dev.biologists.org/lookup/doi/10.1242/dev.185231.supplemental

Peer review history

The peer review history is available online at https://dev.biologists.org/lookup/doi/10.1242/dev.185231.reviewer-comments.pdf.

References

Agre, P., Sasaki, S. and Chrispeels, M. J. (1993). Aquaporins: a family of water channel proteins. *Am. J. Physiol.* **265**, F461. doi:10.1152/ajprenal.1993.265.3.F461

Ameli, P. A., Madan, M., Chigurupati, S., Yu, A., Chan, S. L. and Pattisapu, J. V. (2012). Effect of acetazolamide on aquaporin-1 and fluid flow in cultured choroid plexus. *Acta Neurochir. Suppl.* **113**, 59-64. doi:10.1007/978-3-7091-0923-6_13

Anderson, R. B., Turner, K. N., Nikonenko, A. G., Hemperly, J., Schachner, M. and Young, H. M. (2006). The cell adhesion molecule l1 is required for chain migration of neural crest cells in the developing mouse gut. *Gastroenterology* **130**, 1221-1232. doi:10.1053/j.gastro.2006.01.002

Bin, K. and Shi-Peng, Z. (2011). Acetazolamide inhibits aquaporin-1 expression and colon cancer xenograft tumor growth. *Hepatogastroenterology* **58**, 1502-1506. doi:10.5754/hge11154

Cai, L., Chen, W.-N., Li, R., Hu, C.-M., Lei, C. and Li, C.-M. (2018). Therapeutic effect of acetazolamide, an aquaporin 1 inhibitor, on adjuvant-induced arthritis in rats by inhibiting NF-κB signal pathway. *Immunopharmacol. Immunotoxicol.* **40**, 117-125. doi:10.1080/08923973.2017.1417998

Cao, C., Sun, Y., Healey, S., Bi, Z., Hu, G., Wan, S., Kouttab, N., Chu, W. and Wan, Y. (2006). EGFR-mediated expression of aquaporin-3 is involved in human skin fibroblast migration. *Biochem. J.* **400**, 225-234. doi:10.1042/BJ20060816

Carter, N., Nakamoto, T., Hirai, H. and Hunter, T. (2002). EphrinA1-induced cytoskeletal re-organization requires FAK and p130^{cas}. *Nat. Cell Biol.* **4**, 565-573. doi:10.1038/ncb823

Chen, Y., Rice, W., Gu, Z., Li, J., Huang, J., Brenner, M. B., Van Hoek, A., Xiong, J., Gundersen, G. G., Norman, J. C. et al. (2012). Aquaporin 2 promotes cell migration and epithelial morphogenesis. *J. Am. Soc. Nephrol.* **23**, 1506-1517. doi:10.1681/ASN.2012010079

Chen, J., Wang, Z., Xu, D., Liu, Y. and Gao, Y. (2015). Aquaporin 3 promotes prostate cancer cell motility and invasion via extracellular signal-regulated kinase 1/2-mediated matrix metalloproteinase-3 secretion. *Mol. Med. Rep.* **11**, 2882-2888. doi:10.3892/mmr.2014.3097

Condeelis, J. (1993). Life at the leading edge: the formation of cell protrusions. *Annu. Rev. Cell Biol.* **9**, 411-444. doi:10.1146/annurev.cb.09.110193.002211

Cowan, C. A., Yokoyama, N., Bianchi, L. M., Henkemeyer, M. and Fritzsch, B. (2000). EphB2 guides axons at the midline and is necessary for normal vestibular function. *Neuron* **26**, 417-430. doi:10.1016/S0896-6273(00)81174-5

De Ieso, M. L. and Yool, A. J. (2018). Mechanisms of aquaporin-facilitated cancer invasion and metastasis. *Front. Chem.* **6**, 135. doi:10.3389/fchem.2018.00135

Desban, N. and Duband, J. L. (1997). Avian neural crest cell migration on laminin: interaction of the alpha1beta1 integrin with distinct laminin-1 domains mediates different adhesive responses. *J. Cell Sci.* **110**, 2729-2744.

Desban, N., Lissitzky, J. C., Rousselle, P. and Duband, J. L. (2006). alpha1beta1-integrin engagement to distinct laminin-1 domains orchestrates spreading, migration and survival of neural crest cells through independent signaling pathways. *J. Cell Sci.* **119**, 3206-3218. doi:10.1242/jcs.03057

Ding, T., Ma, Y., Li, W., Liu, X., Ying, G., Fu, L. and Gu, F. (2011). Role of aquaporin-4 in the regulation of migration and invasion of human glioma cells. *Int. J. Oncol.* **38**, 1521-1531. doi:10.3892/ijo.2011.983

Garmon, T., Wittling, M. and Nie, S. (2018). MMP14 regulates cranial neural crest epithelial-to-mesenchymal transition and migration. *Dev. Dyn.* **247**, 1083-1092. doi:10.1002/dvdy.24661

Gustafsson, M. G. L., Shao, L., Carlton, P. M., Wang, C. L. R., Golubovskaya, I. N., Cande, W. Z., Agard, D. A. and Sedat, J. W. (2008). Three-dimensional resolution doubling in wide-field fluorescence microscopy by structured illumination. *Biophys. J.* **94**, 4957-4970. doi:10.1529/biophysj.107.120345

Hamburger, V. and Hamilton, H. L. (1951). A series of normal stages in the development of the chick embryo. *J. Morphol.* **88**, 49-92. doi:10.1002/jmor.1050880104

Hou, B., Zhang, D., Zhao, S., Wei, M., Yang, Z., Wang, S., Wang, J., Zhang, X., Liu, B., Fan, L. et al. (2015). Scalable and DiI-compatible optical clearance of the mammalian brain. *Front. Neuroanat.* **9**, 19. doi:10.3389/fnana.2015.00019

Hu, J. and Verkman, A. S. (2006). Increased migration and metastatic potential of tumor cells expressing aquaporin water channels. *FASEB J.* **20**, 1892-1894. doi:10.1096/fj.06-5930fje

Huber, V. J., Tsujita, M., Yamazaki, M., Sakimura, K. and Nakada, T. (2007). Identification of arylsulfonamides as Aquaporin 4 inhibitors. *Bioorg. Med. Chem. Lett.* **17**, 1270-1273. doi:10.1016/j.bmcl.2006.12.010

Ishibashi, K., Kondo, S., Hara, S. and Morishita, Y. (2011). The evolutionary aspects of aquaporin family. *Am. J. Physiol. Regul. Integr. Comp. Physiol.* **300**, R566-R576. doi:10.1152/ajpregu.90464.2008

Jiang, B., Li, Z., Zhang, W., Wang, H., Zhi, X., Feng, J., Chen, Z., Zhu, Y., Yang, L., Xu, H. et al. (2014). miR-874 Inhibits cell proliferation, migration and invasion through targeting aquaporin-3 in gastric cancer. *J. Gastroenterol.* **49**, 1011-1025. doi:10.1007/s00535-013-0851-9

Karlsson, T., Bolshakova, A., Magalhães, M. A., Loitto, V. M. and Magnusson, K. E. (2013). Fluxes of water through aquaporin 9 weaken membrane-cytoskeleton anchorage and promote formation of membrane protrusions. *PLoS ONE* **8**, e59901. doi:10.1371/journal.pone.0059901

Klebe, S., Griggs, K., Cheng, Y., Driml, J., Henderson, D. W. and Reid, G. (2015). Blockade of aquaporin 1 inhibits proliferation, motility, and metastatic potential of mesothelioma in vitro but not in an in vivo model. *Dis. Markers* **2015**, 286719. doi:10.1155/2015/286719

Lechertier, T. and Hodivala-Dilke, K. (2012). Focal adhesion kinase and tumour angiogenesis. *J. Pathol.* **226**, 404-412. doi:10.1002/path.3018

McKinney, M. C., Fukatsu, K., Morrison, J., McLennan, R., Bronner, M. E. and Kulesa, P. M. (2013). Evidence for dynamic rearrangements but lack of fate or position restrictions in premigratory avian trunk neural crest. *Development* **140**, 820-830. doi:10.1242/dev.083725

McLennan, R. and Kulesa, P. M. (2007). In vivo analysis reveals a critical role for neuropilin-1 in cranial neural crest cell migration in chick. *Dev. Biol.* **301**, 227-239. doi:10.1016/j.ydbio.2006.08.019

McLennan, R., Teddy, J. M., Kasemeier-Kulesa, J. C., Romine, M. H. and Kulesa, P. M. (2010). Vascular endothelial growth factor (VEGF) regulates cranial neural crest migration in vivo. *Dev. Biol.* **339**, 114-125. doi:10.1016/j.ydbio.2009.12.022

McLennan, R., Dyson, L., Prather, K. W., Morrison, J. A., Baker, R. E., Maini, P. K. and Kulesa, P. M. (2012). Multiscale mechanisms of cell migration during development: theory and experiment. *Development* **139**, 2935-2944. doi:10.1242/dev.081471

McLennan, R., Schumacher, L. J., Morrison, J. A., Teddy, J. M., Ridenour, D. A., Box, A. C., Semerad, C. L., Li, H., McDowell, W., Kay, D. et al. (2015a). Neural crest migration is driven by a few trailblazer cells with a unique molecular signature narrowly confined to the invasive front. *Development* **142**, 2014-2025. doi:10.1242/dev.117507

McLennan, R., Schumacher, L. J., Morrison, J. A., Teddy, J. M., Ridenour, D. A., Box, A. C., Semerad, C. L., Li, H., McDowell, W., Kay, D. et al. (2015b). VEGF signals induce trailblazer cell identity that drives neural crest migration. *Dev. Biol.* **407**, 12-25. doi:10.1016/j.ydbio.2015.08.011

McLennan, R., Bailey, C. M., Schumacher, L. J., Teddy, J. M., Morrison, J. A., Kasemeier-Kulesa, J. C., Wolfe, L. A., Gogol, M. M., Baker, R. E., Maini, P. K. et al. (2017). DAN (NBL1) promotes collective neural crest migration by restraining uncontrolled invasion. *J. Cell Biol.* **216**, 3339-3354. doi:10.1083/jcb.201612169

Meng, F., Rui, Y., Xu, L., Wan, C., Jiang, X. and Li, G. (2014). Aqp1 enhances migration of bone marrow mesenchymal stem cells through regulation of FAK and β-catenin. *Stem Cells Dev.* **23**, 66-75. doi:10.1089/scd.2013.0185

Miao, H., Burnett, E., Kinch, M., Simon, E. and Wang, B. (2000). Activation of EphA2 kinase suppresses integrin function and causes focal-adhesion-kinase dephosphorylation. *Nat. Cell Biol.* **2**, 62-69. doi:10.1038/35000008

Morrison, J. A., McLennan, R., Wolfe, L. A., Gogol, M. M., Meier, S., McKinney, M. C., Teddy, J. M., Holmes, L., Semerad, C. L., Box, A. C. et al. (2017a). Single-cell transcriptome analysis of avian neural crest migration reveals signatures of invasion and molecular transitions. *Elife* **6**, e28415. doi:10.7554/eLife.28415

Morrison, J. A., McKinney, M. C. and Kulesa, P. M. (2017b). Resolving in vivo gene expression during collective cell migration using an integrated RNAscope, immunohistochemistry and tissue clearing method. *Mech. Dev.* **148**, 100-106. doi:10.1016/j.mod.2017.06.004

Papadopoulos, M. C., Saadoun, S. and Verkman, A. S. (2008). Aquaporins and cell migration. *Pflugers Arch.* **456**, 693-700. doi:10.1007/s00424-007-0357-5

Parsons, J. T. (2003). Focal adhesion kinase: the first ten years. *J. Cell Sci.* **116**, 1409-1416. doi:10.1242/jcs.00373

Rupp, P. A. and Kulesa, P. M. (2007). High-resolution, intravital 4D confocal time-lapse imaging in avian embryos using a teflon culture chamber design. *CSH Protoc.* **2007**, pdb.prot4790. doi:10.1101/pdb.prot4790

Saadoun, S., Papadopoulos, M. C., Hara-Chikuma, M. and Verkman, A. S. (2005). Impairment of angiogenesis and cell migration by targeted aquaporin-1 gene disruption. *Nature* **434**, 786-792. doi:10.1038/nature03460

Shanahan, C. M., Connolly, D. L., Tyson, K. L., Cary, N. R., Osbourn, J. K., Agre, P. and Weissberg, P. L. (1999). Aquaporin-1 is expressed by vascular smooth muscle cells and mediates rapid water transport across vascular cell membranes. *J. Vasc. Res.* **36**, 353-362. doi:10.1159/000025674

Stroka, K. M., Jiang, H., Chen, S. H., Tong, Z., Wirtz, D., Sun, S. X. and Konstantopoulos, K. (2014). Water permeation drives tumor cell migration in confined microenvironments. *Cell* **157**, 611-623. doi:10.1016/j.cell.2014.02.052

Teddy, J. M. and Kulesa, P. M. (2004). In vivo evidence for short- and long-range cell communication in cranial neural crest cells. *Development* **131**, 6141-6151. doi:10.1242/dev.01534

Tomita, Y., Dorward, H., Yool, A. J., Smith, E., Townsend, A. R., Price, T. J. and Hardingham, J. E. (2017). Role of Aquaporin 1 signaling in cancer development and progression. *Int. J. Mol. Sci.* **18**, 299. doi:10.3390/ijms18020299

Tsygankov, D., Bilancia, C. G., Vitriol, E. A., Hahn, K. M., Peifer, M. and Elston, T. C. (2014). CellGeo: a computational platform for the analysis of shape changes in cells with complex geometries. *J. Cell Biol.* **204**, 443-460. doi:10.1083/jcb.201306067

Verkman, A. S. (2009). Aquaporins: translating bench research to human disease. *J. Exp. Biol.* **212**, 1707-1715. doi:10.1242/jeb.024125

Wei, X. and Dong, J. (2015). Aquaporin 1 promotes the proliferation and migration of lung cancer cell in vitro. *Oncol. Rep.* **34**, 1440-1448. doi:10.3892/or.2015.4107

Woessner, J. F. Jr. (1995). Quantification of matrix metalloproteinases in tissue samples. *Methods Enzymol.* **248**, 510-528. doi:10.1016/0076-6879(95)48033-1

Xiong, G., Chen, X., Zhang, Q., Fang, Y., Chen, W., Li, C. and Zhang, J. (2017). RNA interference influenced the proliferation and invasion of XWLC-05 lung cancer cells through inhibiting aquaporin 3. *Biochem. Biophys. Res. Commun.* **485**, 627-634. doi:10.1016/j.bbrc.2017.02.013

Xu, H., Xu, Y., Zhang, W., Shen, L., Yang, L. and Xu, Z. (2011). Aquaporin-3 positively regulates matrix metalloproteinases via PI3K/AKT signal pathway in human gastric carcinoma SGC7901 cells. *J. Exp. Clin. Cancer Res.* **30**, 86. doi:10.1186/1756-9966-30-86

Zhang, J., An, Y., Gao, J., Han, J., Pan, X., Pan, Y., Tie, L. and Li, X. (2012). Aquaporin-1 translocation and degradation mediates the water transportation mechanism of acetazolamide. *PLoS ONE* **7**, e45976. doi:10.1371/journal.pone.0045976

Supplementary Materials and methods

1 Mathematical model

We use a computational hybrid model based on that presented in McLennan et al. (2012, 2015a,b, 2017). The model is a two-dimensional approximation of the system and consists of a discrete, off-lattice model for the dynamics of neural crest cells that is coupled to a continuum, reaction-diffusion model for the dynamics of chemoattractant (VEGF). We implement the model using Aboria (Robinson, 2017, https://martinjrobins.github.io/Aboria/), a C++ library for particle-based numerical methods.

1.1 Dynamics of cells

We describe briefly how we incorporate the dynamics of cells. We assume that there are two types of cells, namely "leaders" and "followers". Leaders undertake a fixed-jump-length biased random walk up a cell-induced gradient of chemoattractant. To model the cells extending filopodia to sense the concentration of chemoattracant at their tips we simply sample the concentration at a certain number of points a fixed distance away from the center of a cell in randomly chosen directions, and then move the cell in the direction of the highest concentration sensed, provided it is sufficiently higher than the chemoattractant concentration at the position of the center of the cell. If this is not the case, we move the cell in a random direction. On the other hand, followers are either in chains or they move randomly. A chain consists of a group of followers that are close to each other, with at least one of them close to a leader. All the followers in a chain move in the same direction as the leader that is at the front of that chain. If a follower is able to follow more than one cell, i.e. it could join multiple chains, it randomly chooses one to join.

In addition to this model of cell guidance, we implement a simplistic model of tunneling in the extracellular matrix (ECM). Our experimental results show that overexpression of AQP-1 induces an increase in MMP activity which, in turn, results in ECM degradation. In our model we assume that enhanced ECM degradation results in the creation of tunnels in the ECM. We implement a very simplistic model of this tunneling mechanism by recording the history of leader positions, which we define as a "tunnel". If a follower is sufficiently close to a tunnel, then it starts moving along that tunnel towards the front of the stream. If a cell is sufficiently close to more than one tunnel, then it enters the closest tunnel. We assume that guidance via "chains" dominates the tunneling mechanism, i.e. if a follower cell is in a chain then it does not search for a tunnel.

We include phenotype switching based on the position of a cell within a migratory stream. We make a simplification from the previous model by McLennan et al. (2015a) and assume that the phenotype is determined based on cell position rather than VEGF concentration. This simplification is consistent with the experimental observation that gene expression profiles depend on the position of a cell within a migratory stream, with a small number of leaders at the very front of the stream where the concentration of VEGF is the highest (McLennan et al. 2015a). A constant number of leaders is a reasonable as-

sumption in our model because we do not model the system with experimental perturbations in VEGF distribution that have been shown to alter the number of leaders (McLennan et al. 2015b).

1.2 Model assumptions

We now list the key assumptions used in the model. Firstly, we use a fixed time-step model ($\Delta t = 1$min) during which a cell senses its environment and updates its position. Secondly, we model volume exclusion by considering cells as hard-discs that are not allowed to overlap (in reality, cells will deform when they come in contact, so this is a model simplification). If a cell cannot make a movement due to volume exclusion, i.e. the target destination is occupied by other cells, then it remains in the same position. Thirdly, we assume that only the center of the cell has to be inside the rectangular domain (Figure 7H), not the entire cell body. We allow a cell to extend filopodia outside the domain but, in our model, this never leads to a movement in that direction. If all the filopodia of a cell are extended outside the domain and the random direction sampled leads to a movement outside the domain, then the cell does not move. These are the boundary conditions for cells everywhere apart from the neural tube (x = 0) where there is an influx of cells. There is an attempt to insert a new cell at every time step with a center at a random position along the y axis and $x =$ cell radius (that is, the cell is placed fully inside the domain). Lastly, we assume that when cells enter tunnels they move in the direction towards the front of the stream, which means that we assume that there is another guidance cue in tunnels that directs the cells.

1.3 Model features

Filopodia stability, filopodia polarity, filopodia number and ECM degradation rate are new features of the model that we investigate. Filopodia stabilization is implemented here by allowing a leader to sample its environment only every three time steps and in between specifying the cell to move persistently, as opposed to sampling and potentially moving in a different direction each time step. Filopodia polarization entails a leader only stabilizing its filopodium when it makes an informed movement towards a higher concentration of VEGF, as opposed to a movement in a random direction. Filopodia number is the number of random directions a leader samples per time step. We incorporate enhanced ECM degradation by the tunneling mechanism described above, i.e. tunnels generated by the leaders correspond to enhanced ECM degradation. We consider a suite of models to explore the effects of combinations of different experimental perturbations. We label them as “Model x” (x from 1 to 11) and the values of parameters and features for the different models can be found in Table 1.

1.4 Domain

We use a rectangular two-dimensional domain $(x, y) \in [0, L_x(t)] \times [0, L_y]$ as a simplification of a narrow (in height) curved three-dimensional migratory path (Figure 1). We fit the following equation to model the growth of the domain in the x direction:

$$L_x(t) = \frac{L_\infty e^{a(t-t_s)}}{L_\infty / L_0 + e^{a(t-t_s)} - 1} + k_0, \tag{1}$$

with $a = 0.23\text{h}^{-1}\mu\text{m}^{-1}$, $t_s = 15.9\text{h}$, $L_\infty = 867.6\mu\text{m}$, $L_0 = 300.0\mu\text{m}$ and $k_0 = 291.2\mu\text{m}$ inferred from experimental results (McLennan et al. 2012).

1.5 Chemoattractant dynamics

We use a reaction-diffusion equation to model the dynamics of the chemoattractant VEGF based on the work of McLennan et al. (2012, 2015a,b, 2017). We scale the concentration of VEGF, $c(x, y, t)$, to $c \in [0, 1]$ and define the equation on the growing domain with $x \in [0, L_x(t)]$ and $y \in [0, L_y]$ (parameter values in Table 1):

$$\frac{\partial c}{\partial t} = \underbrace{D\left(\frac{\partial^2 c}{\partial x^2} + \frac{\partial^2 c}{\partial y^2}\right)}_{(1)} \underbrace{- c \sum_{i=1}^{N(t)} \frac{\lambda}{2\pi R^2} \exp\left[-\frac{(x-x_i)^2 + (y-y_i)^2}{2R^2}\right]}_{(2)} + \underbrace{\kappa c(1-c)}_{(3)} - \underbrace{\frac{\partial (ac)}{\partial x}}_{(4)}, \tag{2}$$

where D is the diffusion coefficient of the chemoattractant, R is the cell radius, λ is the internalization rate, κ is the production rate of the chemoattractant, a is the flow due to domain growth, $N(t)$ is the number of cells at time t and (x_i, y_i), $i = 1, \ldots, N(t)$ is the position of the center of cell i. We assume zero flux boundary conditions and initial conditions $c(x, y, 0) \equiv 1$. Zero flux boundary conditions are assumed to incorporate a wide and representative stream profile with no loss of chemoattractant from the system. We assume a uniform initial condition based on the observations of McLennan et al. that prior to NC migration VEGF is spatially uniform in the tissue up to the entrance to BA2 (Figure 1) (McLennan et al., 2010).

We briefly explain the reasoning behind the terms on the right-hand side of equation (10). Term (1) corresponds to diffusion of chemoattractant with diffusion coefficient D. Term (2) is the internalization of chemoattractant by cells. We use a simple Gaussian kernel because it takes into account the size of cells, and we assume that the cells consume or degrade chemical with a continually decreasing intensity moving away from the cell center. Term (3) is the production of chemoattractant. We assume logistic production, however, since the production rate, κ, is relatively small in comparison with the internalization rate, λ (see McLennan et al., 2010), the dynamics do not change significantly when other forms of production, such as linear or constant, are considered. Term (4) corresponds to the effect of domain growth. It consists of the advection term, $a \times \partial c/\partial x$, corresponding to elemental areas moving with the flow due to local growth, and a dilution term, $c \times \partial a/\partial x$, due to local area change. Assuming

that the flow can be specified using a growth function Γ, the Lagrangian description is

$$x = \Gamma(X, t), \qquad x \in [0, L_x(t)] \tag{3}$$

where X is an initial position marker, and $\Gamma(X, 0) = X$. The local flow is determined by

$$a(x, t) = \frac{\partial x}{\partial t} = \frac{\partial \Gamma}{\partial t}, \tag{4}$$

(Crampin et al., 1999). Since in our model we assume, for simplicity, that the uniform growth is in one direction (the x direction), the growth function is given

$$\Gamma(X, t) = Xl(t) = x, \qquad l(0) = 1, \tag{5}$$

where $l(t)$ is rescaled domain length, $l(t) = L_x(t)/L_0$ with $L_0 = L_x(0)$. Then the flow is determined by

$$a(x, t) = X\dot{l}(t) = x\frac{\dot{l}(t)}{l(t)}, \tag{6}$$

where $\cdot$ denotes $\mathrm{d}/\mathrm{d}t$. Substituting expression (6) into equation (2), we find

$$\frac{\partial c}{\partial t} = D\left(\frac{\partial^2 c}{\partial x^2} + \frac{\partial^2 c}{\partial y^2}\right) - c\sum_{i=1}^{N(t)} \frac{\lambda}{2\pi R^2} \exp\left[-\frac{(x - x_i)^2 + (y - y_i)^2}{2R^2}\right] + \kappa c(1 - c) - \frac{\dot{l}}{l}\left[x\frac{\partial c}{\partial x} + c\right], \tag{7}$$

We use the following transformation to map the coordinates to the unit interval

$$(x, t) \to (\bar{x}, \bar{t}) = \left(\frac{x}{l(t)}, t\right). \tag{8}$$

Under this mapping

$$\frac{\partial c}{\partial \bar{t}} = \frac{\partial c}{\partial t} + x\frac{\dot{l}}{l}\frac{\partial c}{\partial x}, \tag{9}$$

which leads to the elimination of the advective term in equation (7). Therefore, if we use the transformation (8), but for the sake of simplicity now drop the bars, then equation (7) becomes

$$\frac{\partial c}{\partial t} = D\left(\frac{1}{l(t)^2}\frac{\partial^2 c}{\partial x^2} + \frac{\partial^2 c}{\partial y^2}\right) - c\sum_{i=1}^{N(t)} \frac{\lambda}{2\pi R^2} \exp\left[-\frac{l(t)^2(x - x_i)^2 + (y - y_i)^2}{2R^2}\right] + \kappa c(1 - c) - \frac{\dot{l}(t)}{l(t)}c. \tag{10}$$

Equation (10) is valid on the fixed domain $x \in [0, L_0]$ and $y \in [0, L_y]$. Recall that we assume zero flux boundary conditions and initial conditions $c(x, y, 0) \equiv 1$.

We solve equation (10) using a finite difference method (second-order centred differences in space, and forward Euler in time) with $\Delta x = 10\mu$m, $\Delta y = 10\mu$m and $\Delta t_c = 1$min. These choices are sufficient for the algorithm to have converged and resolve accurately the gradient of VEGF. Note that a time step of 1min is equivalent to the discrete simulation time step for the cell motility model (see Table 1), which is sufficient for the simulations to converge.

1.6 Pseudocode

We provide a pseudocode that explains in detail how we numerically simulate the model. The text in blue corresponds to the steps that are only applicable for the model with a tunneling mechanism included.

The full code is available at https://github.com/rginiunaite/NC-cells.git. We provide two versions of the code: NC-model (Models 1-9), where the interactions between the cells in the NC-model are only by chains; NC-model-tunneling (Models 10,11) where interactions are by both chain and tunneling mechanisms. Note that a user first needs to install the Aboria library (https://martinjrobins.github.io/Aboria/).

Main steps

1. Initialise model parameters and insert N_{leader} leader cells at $x = R$ and equal distance apart in the y direction, set $t = 0$.
2. Choose a random position in y with $x = R$. If there is no overlap with other cells, insert a new follower cell at this position.
3. Solve chemoattractant profile.
4. Grow domain, update cell positions (multiply the position of a cell in the x direction by the ratio of current domain length over the domain length in the previous timestep).
5. Move cells.
6. Implement any phenotype switching.

Internal steps

move cells (Note that if a cell cannot move due to volume exclusion (R - radius of a cell) then the attempted movement is aborted)

1. **for** i = 1 to number of cells **do**
2. pick a cell at random without replacement
3. **if** the cell is a leader, **then**
4. **if** filopodium is stabilized and the cell has not finished moving three steps in the same direction, **then**
move a distance $\Delta t \times \nu$ in the same direction as before **end if**
5. **if** there is no filopodia stability mechanism or the cell has finished moving three steps in the same direction, **then**
6. pick n_{filo} random directions and measure chemoattractant concentration in those random direction(s) at distance l_{filo} away from the center of the cell, pick the highest concentration and set it to c_{new}, measure chemoattractant concentration at the center of the cell and set it to c_{old}
7. **if** $\frac{c_{new}-c_{old}}{\sqrt{c_{old}}} \geq \xi$ (sensing accuracy), **then**
8. move in chosen direction a distance $\Delta t \times \nu$, stabilize filopodium (if stabilization mechanism is on)
9. **end if**
10. **else**
11. move in random direction a distance $\Delta t \times \nu$, stabilize filopodium (if stabilization

mechanism is on and the stabilization is non-polar)
12. **end if**
13. **end if**
14. record the position of a leader if the cell is a distance s apart from the previous position tracked and less than n_t positions are recorded, define it as a "tunnel"
15. **end if**
16. **else** (the cell is a follower)
17. **if** the cell is in a chain, **then**
18. move a distance $\Delta t \times ratio \times \nu$ in the same direction as the leader at the front of the chain
19. **if** the cell is further away than l_{filo}^{max} from the cell which it was following, **then**
20. detach it, and all the cells that were following it, from the chain
21. **end if**
22. **end if**
23. **if** the cell is not in a chain, **then**
24. **if** there is a leader or a follower in a chain less than l_{filo} distance away, **then** join that chain (if there are multiple possibilities, pick one randomly) and move a distance $\Delta t \times ratio \times \nu$ in the same direction as the cell ahead in the chain
25. **end if**
26. **else if** the cell is less than threshold distance d from one of the tunnels (if there are multiple tunnels, pick the closest), **then** move a distance $\Delta t \times ratio \times \nu$ along the tunnel **end if**
27. **else** move a distance $\Delta t \times ratio \times \nu$ in a random direction
28. **end if**
29. **end for**

phenotype switching

1. **if** a cell is a follower **then**
2. **if** the cell is further ahead by ϵ in the x direction than one of the leaders and it is sufficiently close to that leader, **then** swap their phenotypes **end if**
3. **end if**

1.7 Model parameters

We choose most of our parameters based on those from McLennan et al. (2015a,b, 2017). We adapt some of the parameters to recapitulate the experimental results for the control case (Model 1), AQP-1 overexpression (Model 2) and AQP-1 downregulation (Model 3). Table 1 contains the values we used

for the computational results of this paper.

Comments

- We use a fixed-jump-length process where the length of the jump is $\Delta t \times \nu$ for leaders and $\Delta t \times ratio \times \nu$ for followers.

- N_{leader} - number of leaders. We choose a fixed number of five leaders because we find that this is the smallest number of cells that can guide the rest of the population successfully (either by chains or tunnels, results not shown). A higher number of leader cells could be chosen provided that we adjust the internalization rate, the sensing accuracy and the diffusion coefficient to avoid some leaders getting stuck due to the lack of a gradient of chemoattractant.

- $ratio$ - ratio of follower to leader speed. Kulesa et al. (2008) demonstrated that the speed of the followers is higher than that of the leaders. We chose a *ratio* value sufficiently high to ensure that the stream does not break in the control case.

- l_{filo} - sensing radius. We use the value calculated by McLennan et al. (2015) as the sum of the cell radius and the mean filopodial length.

- l_{filo}^{max} - maximum cell separation before contact is lost. We use the value calculated by McLennan et al. (2015), obtained from half of the maximum cell size including filopodium.

- ξ - sensing accuracy. We use the same argument for the accuracy with which the cells can sense a chemical gradient as McLennan et al. (2012, 2015, 2015, 2017). They base their work on the biophysical limit for sensing accuracy derived by Berg and Purcell (1977). Briefly, they assume that fluctuations in molecule number are proportional to $\sqrt{N}$, where N is molecule number. Since we use a continuum variable for the chemoattractant, fluctuations can be expressed as $\sqrt{Ac}$ where A is some area of interest, and c is the average concentration in that area. The inaccuracy of concentration measurements is inversely proportional to fluctuations, which gives

$$\frac{\Delta c}{c} \approx \frac{1}{\sqrt{N}} = \frac{1}{\sqrt{Ac}}. \tag{11}$$

  Rearranging gives

$$\frac{\Delta c}{\sqrt{c}} \approx \xi, \tag{12}$$

  where we define ξ as the sensing accuracy, and $\Delta c = c_{new} - c_{old}$. $\Delta c/\sqrt{c_{old}}$ has to be greater or equal than ξ for the cell to respond. We choose ξ sufficiently high to ensure that movement does not occur in response to very small changes in VEGF concentration. The results are robust if we change this parameter together with the internalization rate λ.

- D - diffusion coefficient of chemoattractant. The exact value of the diffusion coefficient is unknown for the system. We use a relatively small value because it has been shown that only around 1% of VEGF freely diffuses, whilst the rest binds to the ECM (Mac Gabhann et al. 2006). The results are robust to changes in this parameter because it only affects the sharpness of the gradient of VEGF.

Changes in the internalization rate, λ, and the sensing accuracy, ξ, also influence the choice of the diffusion coefficient.

- χ - production rate of chemoattractant. The exact VEGF production rate in the tissue is unknown, but since experimental results show that there is almost no VEGF produced where the cells have already internalized it (McLennan et al. 2010), we assume that the production rate is small.

- λ - chemoattractant internalization rate. The internalization rate is also unknown, we choose this parameter based on the distance traveled by cells in 24h. The results are robust to simultaneous changes in the sensing accuracy, ξ, and the internalization rate, λ, therefore we adapted the internalization rate to our chosen sensing accuracy, ξ.

- ϵ - distance a follower has to be ahead of a leader to swap phenotypes. As discussed in Section 1.4, we use a simplified version of the switching mechanism based on the position in the stream. We assume that a follower has to be $\epsilon = 10\mu$m ahead of a leader for their phenotypes to swap. The results are robust to changes in this parameter because we have a fixed number of leaders.

- d - threshold distance to tunnel to enter it. This parameter has to be chosen carefully with respect to the distance between leader positions that we record, s. It is advisable that d is at most $s/2$, so that a cell is not too close to two tunnel positions at the same time, in which case it randomly chooses which one to start moving along. However, it is unrealistic to choose $d \ll 10\mu$m because we need to incorporate the width of a tunnel.

- s - track spacing. This is a parameter that determines the distance between leader positions that we record, corresponding to a "tunnel". We choose a small value to represent a continuous tunnel on a scale of cell sensing, but not too small to avoid high computational costs. The model is robust to smaller values of s ($s < 20\mu$m), but not for significantly larger values.

- n_t - number of leader positions tracked. We have to choose this parameter sufficiently large so that tunnels extend along the entire domain. We find that if a tunnel is shorter than the length of the domain, then the likelihood of the stream to break is increased.

References

Robinson, M. and Bruna, M. (2017). *Particle-based and meshless methods with Aboria.* SoftwareX, 6:172 – 178.

Crampin E. J., Gaffney E. A., and Maini P. K. (1999). *Reaction and diffusion on growing domains: scenarios for robust pattern formation.* Bulletin of Mathematical Biology, 61(6):1093-1120

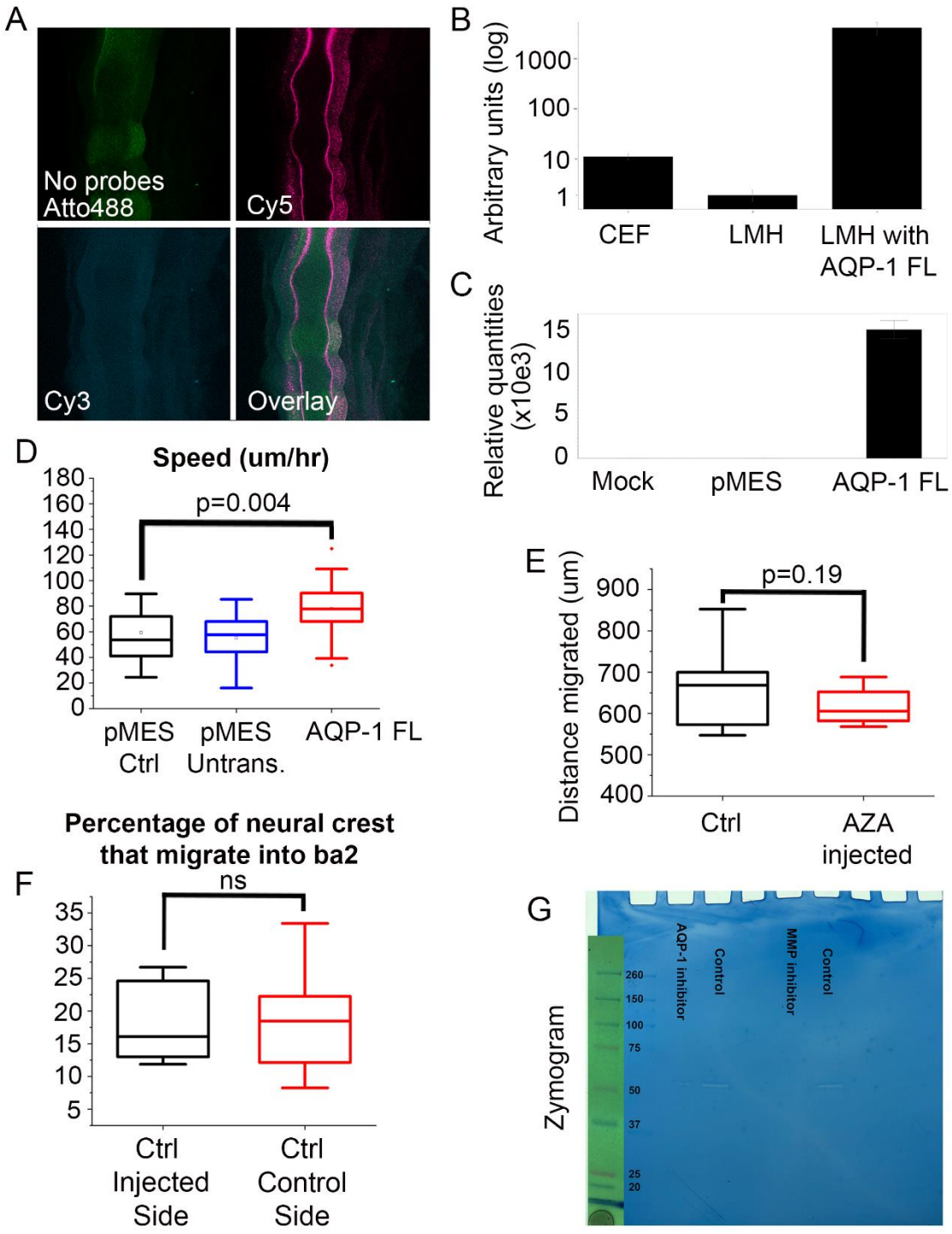

Figure S1. (A) No probes control for RNAscope experiment. (B) Quantification of AQP-1 RNA expression in chick embryonic fibroblasts (CEF), chick liver hepatocellular carcinoma (LMH) and LMH transfected with AQP-1 FL. (C) Quantification of AQP-1 RNA expression in LMH cells after mock transfection, pMES transfection and AQP-1 FL transfection. (D) Box plot of the Speed (microns/hr) of neural crest cells, transfected with pMES control vector (black, n= 27 cells from n=9 neural tube explants), non-transfected but in the same cultures as pMES (blue, n=26 cells) and transfected with AQP-1 FL in different cultures but prepared and imaged the same days as controls (red, n=33 cells from n=10 neural tube explants). (E) Box plot of the distance migrated by neural crest cells after mesodermal injections of AZA (red) and the distance migrated by neural crest cells on the control sides of the same embryos (black), n=6 embryos. (F) Box plot of the percentage of neural crest cells that migrate into the branchial arches, n=8 embryos per treatment. (G) The entire zymogram that is quantified in Figure 5. An image of the ladder (left) was taken prior to development so that it could be clearly seen. Proteins in these assays do not run exactly the same as the markers as enzymes in the samples are not reduced while the markers are (Woessner, 1995). The band size is approximately 62 kD, corresponding to MMP2 (Anderson, 2010).

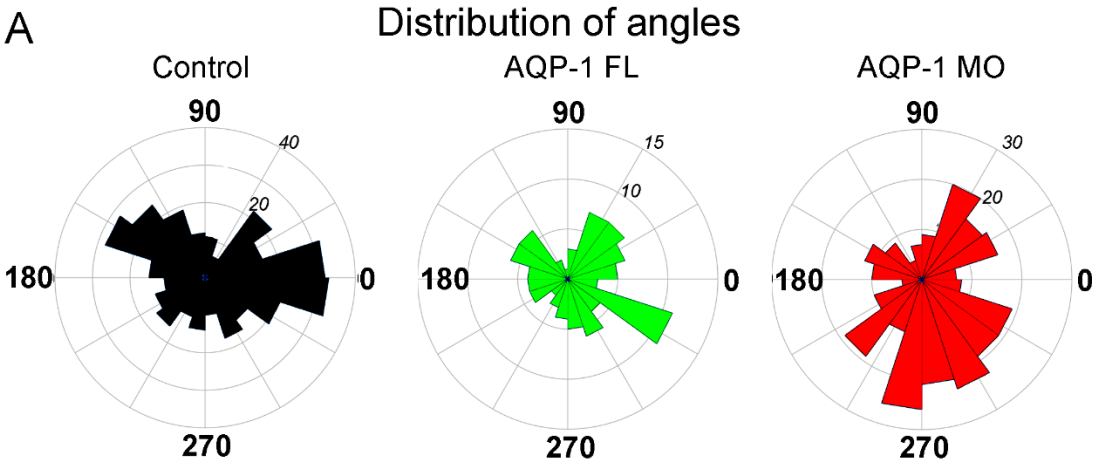

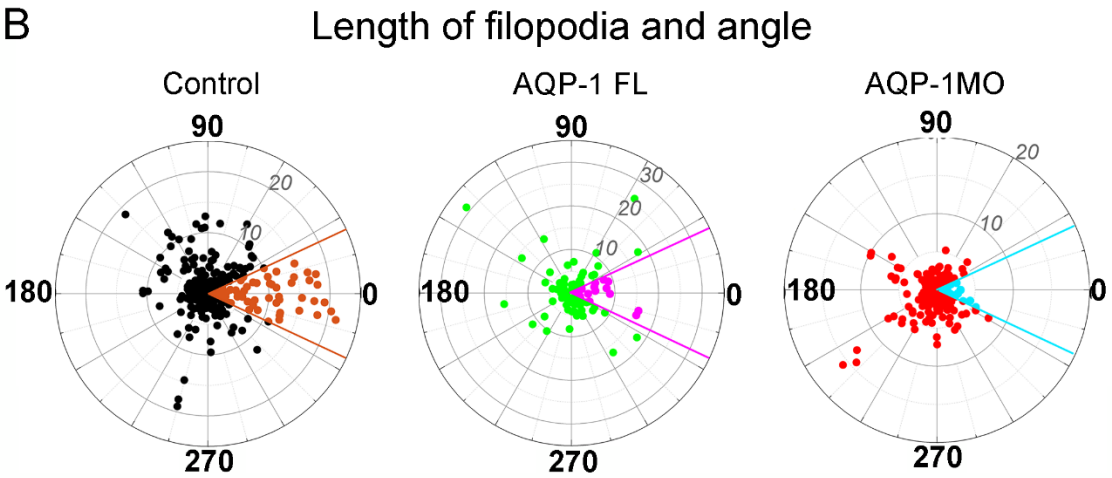

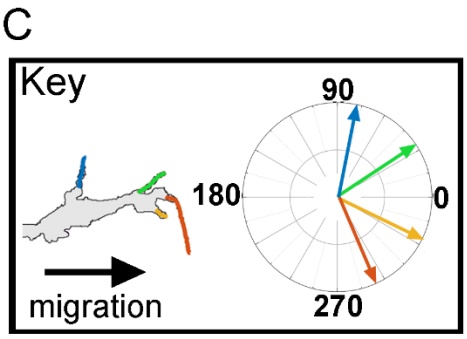

Figure S2: Filopodia direction and length with respect to neural crest migratory direction. (A) Distribution of angles of filopodia for control (black), AQP-1 FL overexpression vector (green) and the AQP-1 MO (red) labeled cells. Radial magnitude equals number of filopodia in that direction. (B) Length and direction of the filopodia for cells labeled with control vector, AQP-1 FL overexpression vector or AQP-1 morpholino. Radial magnitude equals length of the filopodia in microns and angle is with respect to migratory direction. Contrasting colored filopodia are in a 30° window around the direction of migration. (C) Example neural crest filopodia with direction of migration indicated. Direction of migration is always set to 0 degrees.

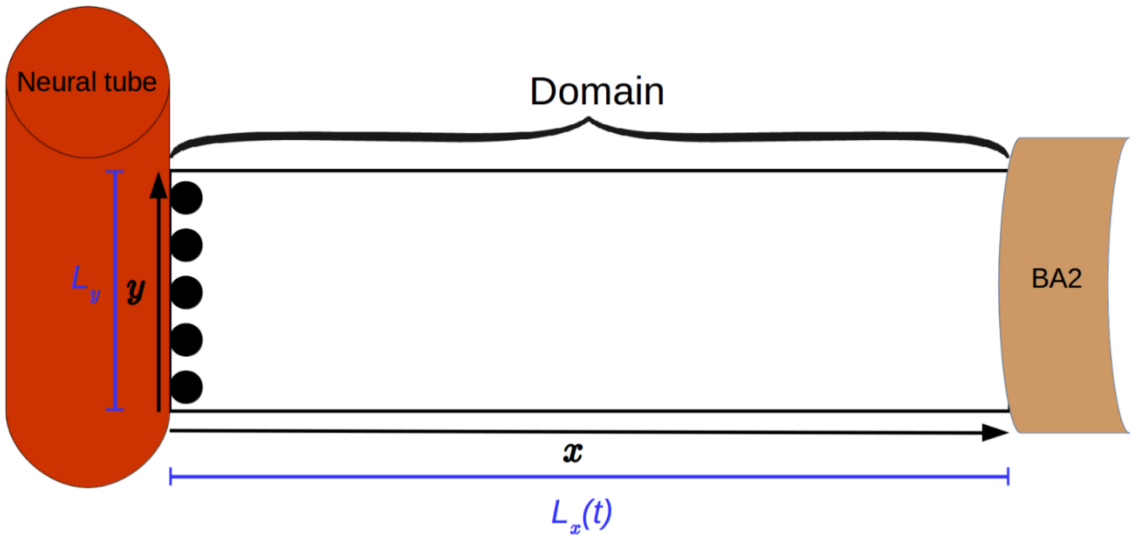

Figure S3: Schematic of a rectangular domain we used to model the domain on which the neural crest cells migrate (black circles). They enter the domain from the neural tube (x = R). BA2 denotes branchial arch 2.

Table S1: Genes that are differentially expressed between pMES (control) and AQP-1 FL.

Click here to Download Table S1

	Description	**Value**	Reference
N_{leader}	number of leaders	5	comments
n_{filo}	directions sampled per time step, filopdia number	1-3	results section
Δt	simulation time step, min	1	n/a
R	cell radius (nuclear), μm	7.5	McLennan and Kulesa (2010)
ν	leader cell speed, μm/h, control case, AQP-1 overexpression and AQP-1 downregulation, respectively	62, 82, 57	results section
$ratio$	ratio of follower to leader speed	1.3	comments
L_y	width of migratory domain, μm	120	McLennan et al. (2012)
$L_x(t)$	length of migratory domain (grows based on eq. (1)), μm	300 to 1100	McLennan et al. (2012)
	Parameters for domain growth equation (1)		
a	growth parameter, h$^{-1}\mu$m^{-1}	0.23	Section 1.1
t_s	growth parameter, h	15.9	Section 1.1
L_∞	growth parameter, μm	867.6	Section 1.1
L_0	initial length of the domain, μm	300	Section 1.1
k_0	growth parameter, μm	291.2	Section 1.1
l_{filo}	sensing radius, μm	27.5	comments
l_{filo}^{max}	maximum cell separation before contact is lost, μm	45	comments
ξ	sensing accuracy	0.1	comments
D	diffusion coefficient of chemoattractant, μm^2/h	0.6	comments
κ	production rate of chemoattractant, /h	0.006	comments
λ	chemoattractant internalization rate, μm$^2/h$	0.02	comments
ϵ	distance a follower has to be ahead of a leader to swap phenotypes, μm	10	comments
	Extra parameters for model with tunneling (Models 10 and 11)		
d	threshold distance to tunnel to enter it, μm	10	comments
s	track spacing, μm	20	comments
n_t	number of leader positions tracked	60	comments

Table S2: Model parameters used in the simulations provided in the results section.

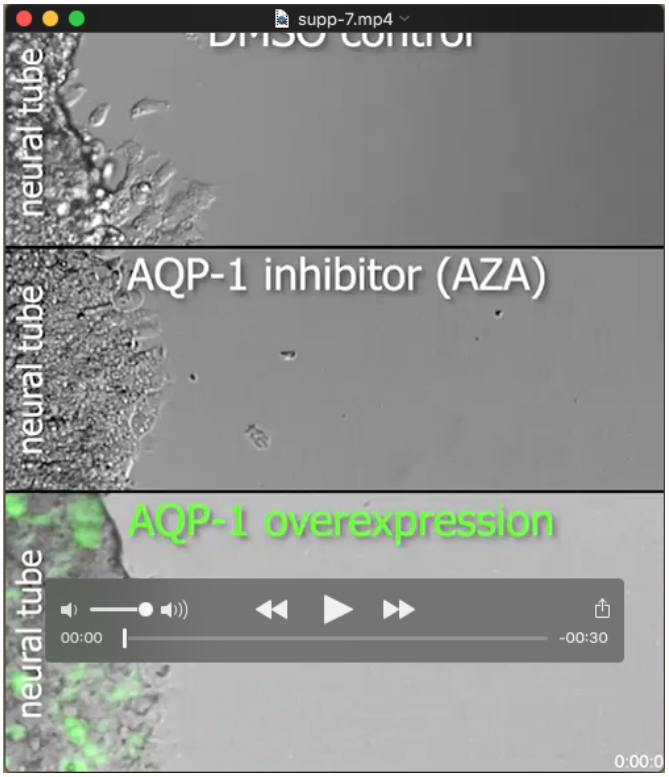

Movie 1: Cranial neural crest cell migratory behaviors are altered in vitro after AQP-1 manipulation. (top) Control migrating neural crest cells exposed to DMSO. (middle) AQP-1 was inhibited by adding Acetazolamide (AZA) to the media. AZA was solubilized in DMSO. (bottom) AQP-1 was overexpressed by transfection of AQP-1 full length construct (green cells). Cranial neural tube explants are shown on the left-hand side of each panel. Time intervals between images ranged from 2.5 to 4 minutes and frame speed was adjusted so that each time-lapse was 8 hours in duration. Scale bar= 30 um.

Movie 2: Cranial neural crest cell migratory behaviors are altered in vivo after AQP-1 manipulation. (Left) Premigratory neural crest cells were transfected with Gap43-YFP/H2B mCherry (control). (Right) AQP-1 full length/H2B mCherry. Z-stacks were collected every 5 minutes and approximately 6 hours is shown. Scale bar= 20 um.

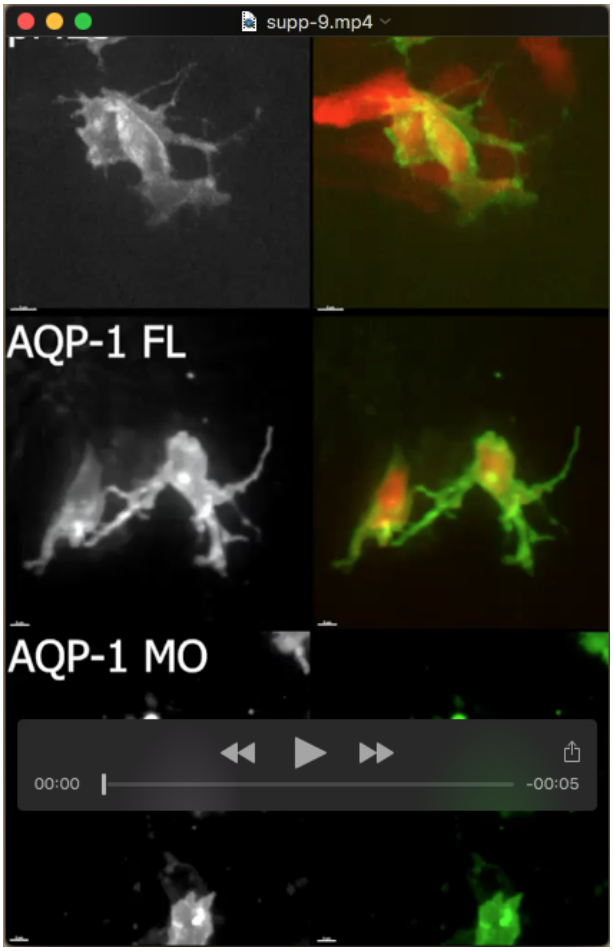

Movie 3: Fast confocal imaging reveals changes in neural crest cell filopodial dynamics after AQP-1 manipulation. Projected images from spinning disk time-lapse microscopy of migrating lead neural crest cells in whole embryo culture electroporated with either (top) pMES control, (middle) AQP-1 FL or (bottom) AQP-1 Morpholino (MO). Each movie sequence shows the cell membrane label (Gap43-mTurquoise2) to highlight the cell protrusion dynamics. Images were collected in 30 second intervals and shown here for approximately 11 min.

Movie 4: Cranial neural crest cell directionality is altered after AQP-1 manipulation. Premigratory neural crest were transfected with pMES (control) or AQP-1 FL and neural tubes were plated in the presence of branchial arch 2 (ba2) tissue as a source of known endogenous chemoattraction. Images were collected every 5 minutes and a total of approximately 18 hours of elapsed time is shown. Scale bar= 50 um.

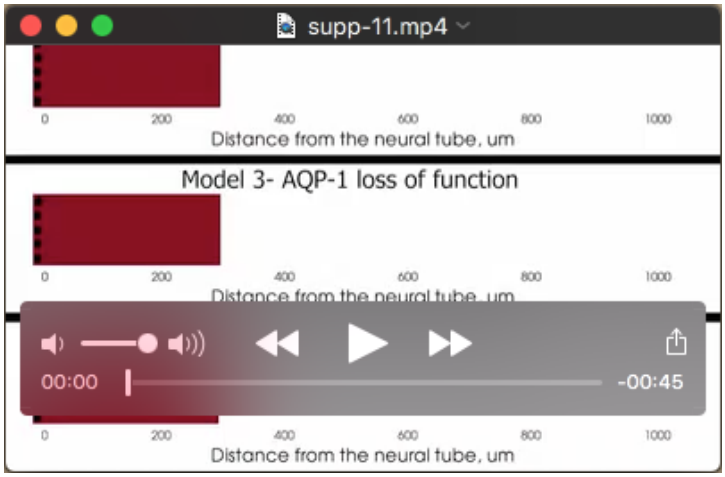

Movie 5: Computer model simulations of cranial neural crest cell migration with AQP-1 manipulation. (top) Control migration is modeled by normal cell speed and unstable filopodia. (middle) AQP-1 loss-of-function is modeled by reduced cell speed and reduced number of cell filopodia. (bottom) AQP-1 gain-of-function is modeled by increased cell speed, stable cell filopodia and tunneling. Each simulation is run on a 2D migratory domain.